journal of the international meteor organization

WGN

47:2
april 2019

Increase of Na layer density with high elevation Geminid radiant
Single-observer meteor velocity calculation with forward scatter
Automated spectrogram analysis for meteor head echoes
March-April IMO video meteors

ISSN 1016-3115

WGN Vol. 47, No. 2, April 2019, pp. 43 – 74

Original research article

Radio meteors

Preliminary results

Front cover photo

This impressive fireball was captured while photographing aurora on 2019 February 8 at $03^{h}15^{m}$ UT from Sandgerði, Iceland. Photo courtesy: Oliver Staiger.

Back over photo

Single station shower association plot from 2018 December 14, the peak night of the Geminids. Meteors were captured using one IMX291 camera with a 3.6 mm $f/0.95$ lens from a station in Hum, Croatia. Credit: Denis Vida, Aleksandar Merlak.

Writing for WGN

This Journal welcomes papers submitted for publication. All papers are reviewed for scientific content, and edited for English and style. Instructions for authors can be found in WGN **45:1**, 1–5, and at `http://www.imo.net/docs/writingforwgn.pdf` .

Copyright

Legal address

International Meteor Organization, Jozef Mattheessensstraat 60, 2540 Hove, Belgium.

Original research article

Responses of mesospheric sodium layer to the Geminids meteor shower activities observed with a resonance scattering lidar located in northern mid-latitude in 2007 and 2008

Mitsumu K. Ejiri[1,2], *Takuji Nakamura*[1,2], *Yasunori Fujiwara*[1], *Takuya D. Kawahara*[3]

The impact that the Geminid meteor shower has on the sodium (Na) layer density at an altitude range of 90–100 km between 262.0° and 263.0° solar longitude was observed with a resonance scattering lidar at Uji (34.9°N, 135.8°E) in 2007 and 2008. With an increase in the elevation angle of the Geminid radiant point, the altitude of the maximum Na density descended from 97 km to 90 km and the maximum density quadrupled. Nightly variation of the Na column density showed an exceptional increase over five hours when the elevation angle of the Geminid radiant point was larger than $\sim 60°$ on December 14, 2007 and 2008. The large elevation angle was likely to be required for a prominent increase in the Na column density although a physical meaning for the threshold is still under investigation. In addition, the Na column density variation as a function of the solar longitude clearly showed that the meteoric Na flux is greater after the Geminid meteor shower peak determined by visual and radio meteor observations.

Received 2019 January 13

1 Introduction

The major source of metals in the mesosphere-lower thermosphere (MLT) is known to be due to the vaporization of meteoroid constituent minerals (Plane, 2003). However, the input flux of meteoroids into the atmosphere is rather uncertain because it is difficult to observe the meteoroids with the wide mass range from approximately 10^{-10} to 10^{2} g (Ceplecha et al., 1998) with a single technique. Meteoroids are usually defined as their sizes (diameters) ranging from 30 micrometers and 1 meter. However, the number of meteoroids with masses ranging from between $\sim 10^{-10}$ and 10^{-5} g and between $\sim 10^{-5}$ and 10^{2} g can be estimated from the radio and optical meteor observations, respectively. However, calibration and cross-validation of these techniques have not been fully successful yet. Moreover, measurement techniques for the meteoroid constituent metals are limited. The optical spectral observation of meteors is one technique that can detect meteoroid constituent metals. A recent development in sensitive video observation techniques has enabled the detection of much more numbers of meteor spectra in comparison with using only photo observation (e.g., Borovička et al., 2005). However, these techniques provide only the relative mixing ratios of the constituent metals, not absolute quantities.

A resonance scattering lidar can measure the density profiles of metal atoms and ions, such as Na, Fe, K, Ca, and Ca^{+}, in the MLT region with high time and range resolution. Meteor trails are sometimes detected by lidar measurements with an integration time of several seconds or less as a high-density thin layer (e.g., von Zahn et al., 1999; Dunker et al., 2013; 2015; Liu et al., 2014; Ejiri et al., 2019); metal abundances in the meteor trails have been estimated via such observations.

To recognize the impact of meteor showers on the metallic layers in the MLT region, temporal variations in the metal column density have been observed for known meteor showers such as the Perseids, Leonids, Geminids, etc. Some authors have found a positive correlation between column density changes and meteor shower activity (Hacke Jr. et al., 1972; Mégie & Blamont, 1977; Uchiumi et al., 1993; Gerding et al., 1999; Höffner et al., 1999) while others have reported no significant correlation (Chu et al., 2000; Höffner et al., 2000; Liu & Yi, 2004; Dunker et al., 2013; Dunker et al., 2015). The presence or absence of impact remains an unanswered question. Höffner and Friedman (2004) investigated seasonal variations within metal layers of K, Ca, Fe and Na observed at two sites, Kühlungsborn (54.1°N, 11.8°E) and Arecibo (18.3°N, 66.7°W), with focusing on known meteor showers and sporadic meteor activity. As a result, they contended that a direct influence from ablating meteoroids appeared on the topside of the mesospheric metal layer at above 110 km, rather than on the average metal layer in the altitude range of 80–105 km. However, metallic atoms above 95 km are mostly converted to metallic ions via ion chemistry (Plane, 2004), so the density of metallic atoms above 110 km is much less than in the average layers and contributes only a little to metal column densities. Thus, only the increase in the density of metallic atoms above 110 km cannot explain the previous observations that have shown a positive correlation between column density change and meteor shower activity.

In this study, we will demonstrate that the Na flux from the Geminid meteor shower can be detected by considering the elevation angle of the Geminid radiant point and show the solar longitude dependency of Na flux by the Geminid meteor shower.

[1]National Institute of Polar Research, 10-3, Midoricho, Tachikawa, Tokyo 190-8518, Japan.
[2]SOKENDAI (Department of Polar Science, The Graduate University for Advanced Studies), 10-3, Midoricho, Tachikawa, Tokyo 190-8518, Japan.
[3]Shinshu University Faculty of Engineering, 4-17-1, Wakasato, Nagano 380-8553, Japan.

IMO bibcode WGN-472-ejiri-lidar
NASA-ADS bibcode 2019JIMO...47...43E

2 Observation

The resonance scattering lidar, developed by the National Institute of Polar Research (NIPR) and Shinshu University for an Antarctic observation project in 1998, measured the sodium (Na) density and temperature profiles in the mesosphere and lower thermosphere (MLT) region (∼ 80–105 km altitude range) using a two-frequency technique (She et al., 1990). The lidar transmitter is composed of two injection-seeded, pulsed Nd:YAG lasers with wavelengths of 1064 nm and 1319 nm. The Na resonance line radiation at 589 nm was produced by a sum frequency generator with a nonlinear crystal (beta-barium borate, BBO) (Jeys et al., 1989). Repetition of the laser pulse was 10 Hz and the output energy was ∼ 25 mJ. The beam divergence of the transmit laser was adjusted to < 1 mrad. The resonance scatter signal was received by a 50-cm diameter Dall-Kirkham Cassegrain telescope with an operational field of view (FOV) of 1–2 mrad. Details were given in Kawahara et al. (2011).

The lidar observation was conducted at the Research Institute for Sustainable Humanosphere (RISH), Kyoto University in Uji, Japan (34.9°N, 135.8°E) from October 2007 to January 2009. The Na density and the MLT temperature profiles were obtained for 136 nights (more than 1200 hours) (Ejiri et al., 2010). Na density profiles were derived every hour with a vertical resolution of 2.0 km, and then the Na column density was calculated as an integration of the Na densities in an altitude range from 70 km up to 120 km. The irradiated area by our transmit laser was smaller than 100 m diameter around the zenith at 100 km altitude and the volume in which Na column density for 70–120 km altitude was measured was smaller than 0.43 km^3.

Figure 1a shows nightly variations of the hourly Na column densities observed in 2008. Red dots connected with a solid red line indicate the Na column density variation on 2008 December 14. Results from the other 105 nights are plotted with black solid lines and mean values using blue dots connected with a solid blue line. Two standard deviations (2-sigma) are illustrated with blue vertical error bars; the blue dashed lines show standard deviations (1-sigma). The Na column density between 15^h and 19^h UT on December 14 increased significantly, with column density surprisingly higher than the mean curve, exceeding the calculated 2-sigma trend. Hourly temperature averaged for the altitude range of 88–98 km is shown in Figure 1b. The variation in temperature during the night of 2008 December 14, plotted by red dots connected with a solid red line, was similar to the average variation in 2008, plotted by blue dots connected with a solid blue line. The amplitude of the variation on December 14 was within 1-sigma when comparing to mean values.

Figure 2a shows a height-time plot of the Na density between 80 km and 105 km. The maximum Na density in the Na layer was 3.3×10^3 cm^{-3} before 11^h UT. This increased over time and reached 13.8×10^3 cm^{-3} at 16^h UT. After that, it decreased to 4×10^3–5×10^3 cm^{-3} at 19^h UT. The altitude of the maximum Na density descended from 97 km at 10^h UT to 90 km at 18^h UT and

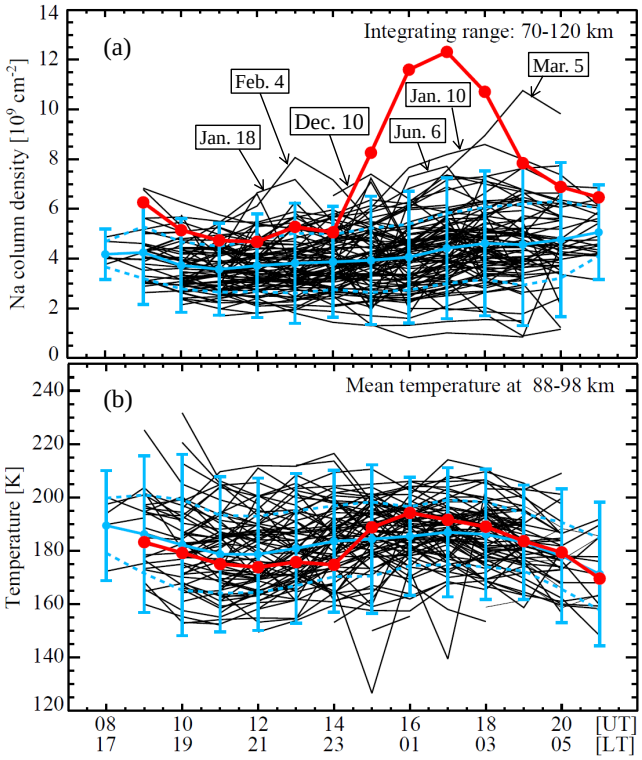

Figure 1 – Nightly variations of (a) Na column density and (b) temperature averaged in the altitude range of 88–98 km. Local time (LT) is universal time (UT) plus 9 hours. The red dots connected with a red polygonal line show the data on 2008 December 14. The observed data and mean from the other 105 nights in 2008 are shown by the black lines and the blue dots connected with a blue polygonal line, respectively. The blue vertical bars represent 2-sigma. 1-sigma is shown by the blue dashed lines.

returned to a high-altitude of 96 km at 19^h UT. The Na layer with a density greater than 3×10^3 cm^{-3} extended from an altitude of 96 km at 11^h UT to 83 km at 19^h UT while the top of the layer was almost constant at ∼ 99 km. From 15^h UT to 19^h UT when the high column densities were observed, Na densities were found to be enhanced over a wide range of ∼ 10 km (between 88 and 98 km altitude). The elevation angle of the Geminid radiant point at Uji is plotted in Figure 2b. It was larger than 60° between 14^{h}32^m UT and 19^{h}23^m UT. The height-time plot of temperature between 80 km and 105 km is displayed in Figure 2c. The altitude of the highest temperature descended from 100 km at ∼ 14^h UT to 80 km at ∼ 19^h UT. The descent was likely to be associated with an atmospheric wave with a wave period of 8–10 hours. This descent was at a different rate from the descent in altitude of the maximum Na density.

As a comparison with these variations on 2008 December 14, Figure 3 shows typical variations of Na density and temperature during the night in winter due to atmospheric waves on 2008 January 10. The temperature variation in Figure 3b clearly shows downward phase propagation with a wave period of 8–10 hours. The Na density variation in Figure 3a shows the Na layer is descending with the downward phase propagation in temperature especially after 11^h UT. The Na density at around 90 km altitude increased by

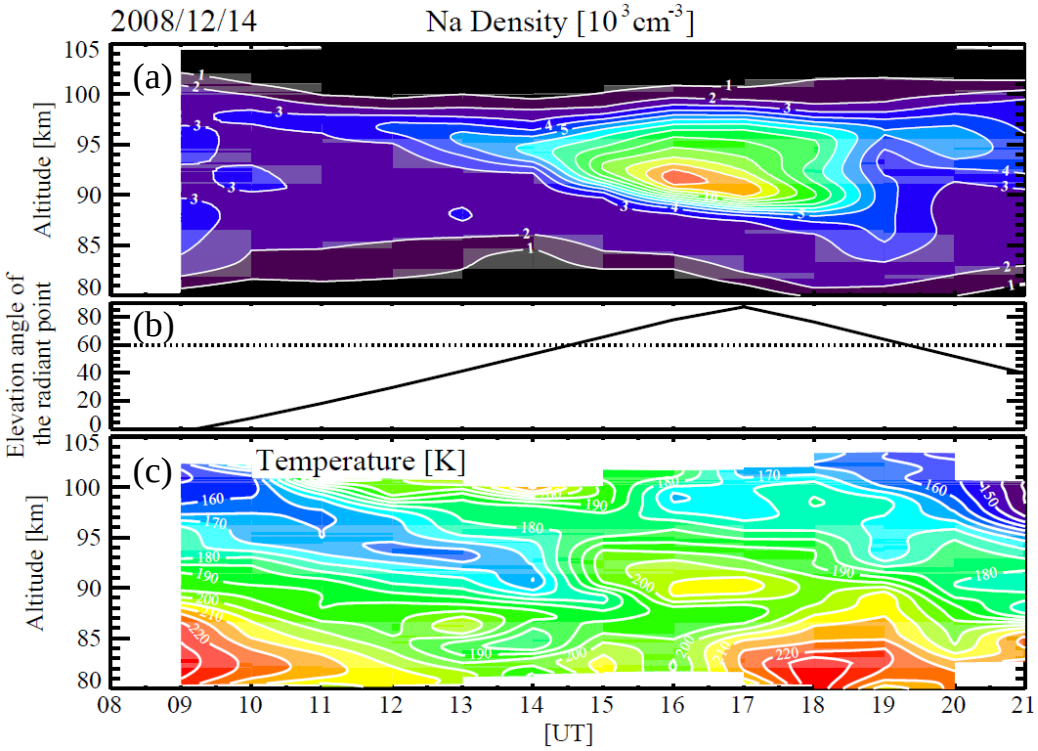

Figure 2 – Height-time plots of (a) Na density and (c) temperature observed on 2008 December 14. (b) Elevation angle variation of the Geminid radiant point at Uji on 2008 December 14, is plotted by a solid line as a function of time. A horizontal dashed line indicates an elevation angle of 60°.

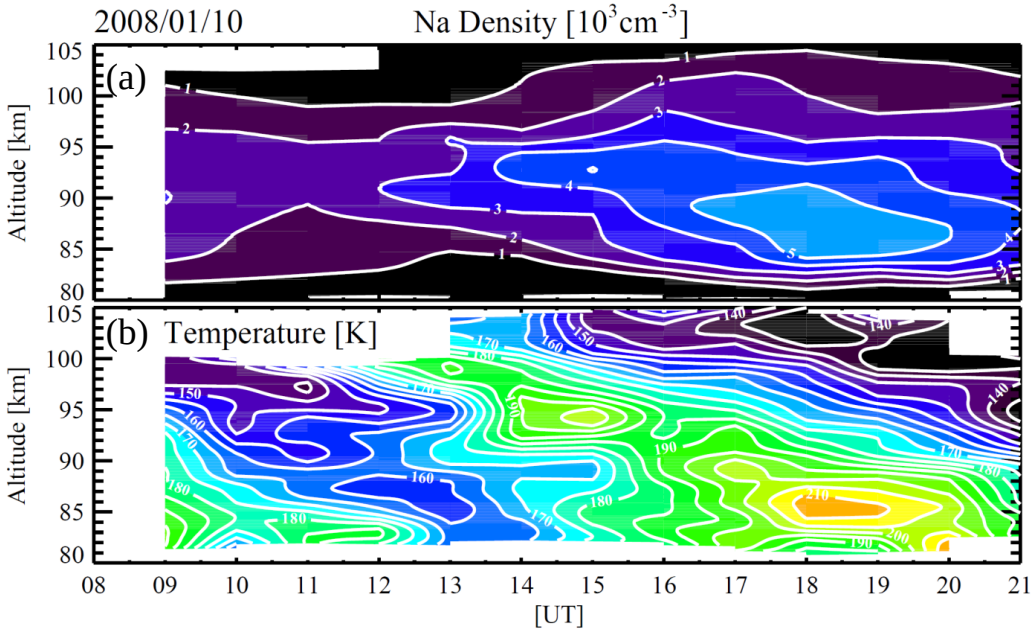

Figure 3 – Height-time plots of (a) Na density and (b) temperature observed on 2008 January 10.

2×10^3 cm^{-3} with a temperature increase of 25 K caused by the atmospheric wave. In contrast, the Na density in Figure 2a increased by 10×10^3 cm^{-3} when the temperature increased by 25 K at around 90 km altitude. This extraordinary increase cannot be explained by the temperature variation and requires another source of Na.

3 Discussions

3.1 Correlation between the Na column density and the elevation angle of the Geminid radiant point

The Na column density significantly increased between 15^h and 19^h UT on December 14 when the elevation angle of the Geminid radiant point was larger

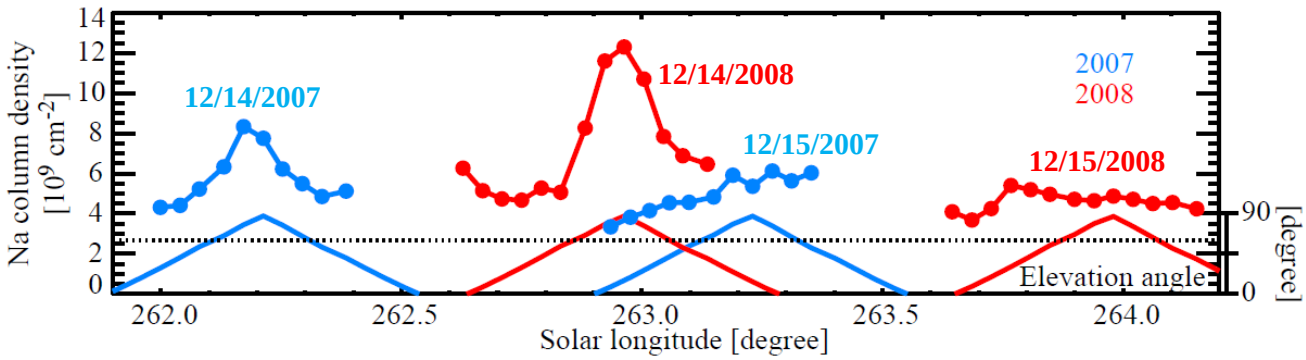

Figure 4 – Temporal variations of the Na column densities and elevation angles of the Geminid radiant point as a function of the solar longitude, shown by solid lines with and without dots, respectively. Blue is for 2007 and red is for 2008.

than $\sim 60°$. Uchiumi et al. (1993) pointed out a positive correlation between Na column density and the elevation angle of the Perseid radiant point observed at Fukuoka, Japan (33.4°N, 130.2°E) in 1981 and 1983. Our observations clearly showed not only a similar correlation but also the importance of a large elevation angle ($>\sim 60°$) of the Geminid radiant point for a Na column density increase. When an exceptionally massive fireball ablation occurs within the lidar FOV, quite strong resonance scatter signal may be detected. However such strong signals were not seen in every single profile obtained by compiling 1500 laser shots (150 s integration time) during the observation on December 14, 2007 and 2008. Hence, the observed increase of Na column density (seen in Figure 1a) was not caused by a few exceptionally massive fireballs. The apparent descent of the Na layer with an increasing elevation angle of the Geminid radiant point in Figure 2a could be explained by the fact that higher radiant point causes a deeper penetration of meteoroids. Additionally, the Na density became quite high around culmination, which can be explained by a much longer chemical lifetime of Na between 90 and 95 km than the other altitude (Gardner & Liu, 2010; Plane, 2004). Therefore, such a large elevation angle of the radiant point ($>\sim 60°$) is likely to be required for penetration of meteoroids down to the altitude range of 90–95 km that induce a prominent increase in the Na column density.

Liu and Yi (2004) concluded that the 2001 Leonid meteor shower did not have a significant impact on the Na abundance in the MLT region from a day-to-day variation in nightly mean Na column densities observed by a Na lidar at Wuhan (30.5°N, 114.4°E). However, they observed that the Na densities at around 85–105 km altitude increased significantly after $\sim 04^{h}30^{m}$ LT ($\sim 20^{h}30^{m}$ UT) in a height-time plot of Na density (see Figure 1 in Liu and Yi, 2004). The elevation angle of the Leonid radiant point at Wuhan was larger than $\sim 60°$ from $04^{h}40^{m}$ LT to $08^{h}50^{m}$ LT and culminated at 81.2° at $06^{h}45^{m}$ LT. Therefore, the Na density was likely to have increased when the elevation angle of the Leonid radiant point was significantly large.

3.2 The solar longitude dependence of Na flux by the Geminid meteor shower

The Na column density over Uji on December 14 increased with larger elevation angles of the Geminid radiant point not only in 2008 but also in 2007. The Geminids is one of the permanent meteor showers currently visible and year-to-year differences in the activity and period observed by visual and radio meteor observations are known to be small (e.g., Rendtel, 2004). Nightly variations of hourly Na column density observed on December 14 and 15 in 2007 and 2008 are displayed in Figure 4 as a function of solar longitude. The elevation angles of the Geminid radiant point for these nights are also shown at the lowest part of the same figure. A horizontal dotted line indicates an elevation angle of $\sim 60°$. The Na column densities on December 14 in 2007 also increased with an increasing elevation angle of the Geminid radiant point, especially when it was larger than $\sim 60°$. On the other hand, the nightly variation of the Na column densities observed on December 15 in both years, 2007 and 2008, did not show such a clear increase. The active period of the Geminid meteor shower is from 260° to 264° in solar longitude with a peak of the activity between 261.5° and 262.4° (Rendtel, 2004). The activity increases gradually and decreases rapidly. In Figure 4, the Na column densities on December 14 in 2008 showed a significant increase but those on December 15 in 2007 did not show such a clear increase despite observations at similar solar longitudes to those showing significant activity on December 14 in 2008. Between 260° and 262° in solar longitude, our lidar data was absent because of bad weather.

Moreover, the maximum Na column densities during the night of December 14 in 2008 was 12.3×10^{9} cm^{-2} at a solar longitude of 262.96°, 17^{h} UT, which was greater than the 8.3×10^{9} cm^{-2} obtained at 262.17°, 16^{h} UT, on December 14 in 2007. Ryabova and Rendtel (2018) reported that from 1985 to 2016 the Geminids meteor shower activity increased gradually with a yearly increment of 1.79 in the maximum zenith hourly rate (ZHR) in the solar longitude period of 261°–262° by analysis of visual observations. The maximum ZHR for 2008 seems apparently larger than the other years around

2008 and is $\sim 30\%$ larger than that for 2007. On the other hand, the maximum Na column density for 2008 was $\sim 50\%$ larger than that for 2007, which could not be solely explained by the difference, $\sim 30\%$, in the Geminids activity between 2007 and 2008. According to the activity of the Geminids derived from the visual meteor database of the International Meteor Organization (IMO), the ZHR of the Geminids at 263.0° is approximately quarter of a peak ZHR around 262.2° while the maximum ZHR for brighter meteor, i.e. meteors with larger meteoroids, is appeared at later solar longitude (Uchiyama, 2010). For example, the maximum ZHR for the meteor magnitude of +3 appeared at 262.2° and those for the meteor magnitude of −5.6 were shown at 262.7°. Therefore, our observation results indicate that the Na flux at later solar longitude where is thought to have larger dust grains was greater than that at the Geminid meteor shower peak.

The 2010 Geminid meteor shower was concluded to have no contribution to the Na abundance in the MLT region by Dunker et al. (2013). The Na abundance was observed at the Arctic Lidar Observatory for Middle Atmosphere Research (ALOMAR) (69.3°N, 16.0°E) for 12 nights in total in December from 2009 to 2011. Most nights were before 260.8° or after 263.6° in the solar longitude. At the only night around 263.1°, however, the elevation angle of the Geminid radiant point was smaller than 20° during the observation. Their results can be explained by our finding that a prominent increase in the Na column density requires large elevation angle of the radiant point at later solar longitude at the Geminid meteor shower peak.

The Geminid meteoroid stream is known to be composed of meteoroids with varying contents of Na (Borovička et al., 2005). To be entirely clear, the solar longitude dependency of Na flux by the Geminid meteor shower requires more such lidar observations between 260.0° and 263.0° at the latitudes where the elevation angle of the Geminid radiant point becomes larger than $\sim 60°$.

4 Conclusion

The impact of the Geminid meteor shower of the Na layer in the MLT region was investigated using Na lidar measurements on December 14 and 15 in 2007 and 2008 at Uji, Japan. With rising elevation angle of the Geminid radiant point from zero to 87.2° on 2008 December 14, the maximum Na density increased from 3.3×10^3 cm^{-3} to 13.8×10^3 cm^{-3} and its altitude descended from 97 km to 90 km. Additionally, the hourly Na column density showed a significant increase when the elevation angle of the Geminid radiant point was larger than $\sim 60°$. Although a physical explanation for the threshold ($\sim 60°$) is still under investigation, such large elevation angle of the radiant point is likely to be required for a prominent increase in the Na column density.

The Na column density variation as a function of the solar longitude clearly showed that the Na column density increase at a solar longitude of 262.96° is greater than that at 262.17°. This fact reveals that the meteoric Na flux is larger after the Geminid meteor shower peak determined by visual and radio meteor observations.

Our lidar measurements demonstrated that the hourly Na density profiles can detect the Na flux of the Geminid meteor shower by considering the elevation angle of the Geminid radiant point. Such lidar measurements will be useful for the estimation of total Na flux from a meteor shower that is composed of meteoroids with a variable content of Na, like the Geminids.

Acknowledgements

M. K. Ejiri received support as a Japan Society for the Promotion of Science Postdoctoral Fellow (JSPS grant 19-792). This study was also partially supported by the Grants-in-Aid for Scientific Research (A) (Grant Number 15H02137) and (B) (Grant Numbers 18340152, 20403011, 21340141, and 24340121) from the JSPS and by the Center for the Promotion of Integrated Sciences (CPIS) of Sokendai. The authors gratefully acknowledge the use of the Research Institute for Sustainable Humanosphere (Kyoto University) and the Na temperature lidar (Shinshu University) for this observation. The lidar data can be accessed at the following URL: `http://id.nii.ac.jp/1291/00015413/`. The production of this paper was supported by an NIPR production subsidy.

References

Borovička J., Koten P., Spurný P., Boček J., and Štork R. (2005). "A survey of meteor spectra and orbits: Evidence for three populations of Na-free meteoroids". *Icarus*, **174**, 15–30.

Ceplecha Z., Borovicka J., Elford W. G., Revelle D. O., Hawkes R. L., Porubcan V., and Simek M. (1998). "Meteor phenomena and bodies". *Space Sci. Rev.*, **84**, 327–471.

Chu X., Pan W., Papen G., Gardner C. S., Swenson G., and Jenniskens P. (2000). "Characteristics of Fe ablation trails observed during the 1998 Leonid meteor shower". *Geophys. Res. Lett.*, **27**, 1807–1810.

Dunker T., Hoppe U.-P., Stober G., and Rapp M. (2013). "Development of the mesospheric Na layer at 69° N during the Geminids meteor shower 2010". *Ann. Geophys.*, **31**, 61–73. `https://doi.org/10.5194/angeo-31-61-2013`.

Dunker T., Hoppe U.-P., Stober G., and Rapp M. (2015). "Corrigendum to "Development of the mesospheric Na layer at 69° N during the Geminids meteor shower 2010", published in Ann. Geophys. 31, 61-73, 2013". *Ann. Geophys.*, **33**, 197. `https://doi.org/10.5194/angeo-33-197-2015`.

Ejiri M. K., Nakamura T., and Kawahara T. D. (2010). "Seasonal variation of nocturnal temperature and sodium density in the mesopause region observed by a resonance scatter lidar over

Uji, Japan". *J. Geophys. Res.*, **115**, D18126. https://doi.org/10.1029/2009JD013799.

Ejiri M. K., Nakamura T., Tsuda T. T., Nishiyama T., Abo M., Takahashi T., Tsuno K., Kawahara T. D., Ogawa T., and Wada S. (2019). "Vertical fine structure and time evolution of plasma irregularities in the Es layer observed by a high-resolution Ca+ lidar". *Earth, Planets and Space*, **71:3**. https://doi.org/10.1186/s40623-019-0984-z.

Gardner C. S. and Liu A. Z. (2010). "Wave-induced transport of atmospheric constituents and its effect on the mesospheric Na layer". *J. Geophys. Res.*, **115**, D20302. https://doi.org/10.1029/2010JD014140.

Gerding M., Alpers M., Höffner J., and von Zahn U. (1999). "Simultaneous K and Ca lidar observations during a meteor shower on March 6/7, 1997, at Küuhlungsborn, Germany". *J. Geophys. Res.*, **104**, 24689–24698.

Hacke Jr. R. D., Arnold D. E., Jackson D. W., Evans W. E., Ficklin B. P., and Long R. A. (1972). "Dye-laser observations of the nighttime atomic sodium layer". *J. Geophys. Res.*, **77**, 6839–6848.

Höffner J., Fricke-Begemann C., and von Zahn U. (2000). "Note on the reaction of the upper atmosphere potassium layer to the 1999 leonid meteor storm". *Earth, Moon and Planets*, **82**–**83**, 555–564.

Höffner J. and Friedman J. S. (2004). "The mesospheric metal layer topside: A possible connection to meteoroids". *Atmos. Chem. Phys.*, **4**, 801–808. https://doi.org/10.5194/acp-4-801-2004.

Höffner J., U. von Zahn W. J. M., and Murad E. (1999). "The 1996 Leonid shower as studied with a potassium lidar: Observations and inferred meteoroid sizes". *J. Geophys. Res.*, **104**, 2633–2643.

Jeys T. H., Brailove A. A., and Mooradian A. (1989). "Sum frequency generation of sodium resonance radiation". *Appl. Opt.*, **28**, 2588–2591.

Kawahara T. D., Kitahara T., Kobayashi F., Saito Y., and Nomura A. (2011). "Sodium temperature lidar based on injection seeded Nd:YAG pulse lasers using a sum-frequency generation technique". *Optics Express*, **9:4**, 3553–3561.

Liu J. and Yi F. (2004). "Sodium resonance lidar observations during 2001 Leonid meteor shower over Wuhan". *Chin. Sci. Bull.*, **49**, 303–306. https://doi.org/10.1007/BF03182816.

Liu Y. J., Plane J. M. C., Clemesha B. R., Wang J. H., and Cheng X. W. (2014). "Meteor trail characteristics observed by high time resolution lidar". *Ann. Geophys.*, **32**, 1321–1332. https://doi.org/10.5194/angeo-32-1321-2014.

Mégie G. and Blamont J. E. (1977). "Laser soundings of atmospheric sodium interpretation in terms of global atmospheric parameters". *Planet. Space Sci.*, **25**, 1093–1109.

Plane J. M. C. (2003). "Atmospheric chemistry of meteoric metals". *Chem. Rev.*, **103:12**, 4963–4984.

Plane J. M. C. (2004). "A new time-resolved model of the mesospheric Na layer: Constraints on the meteor input function". *Atmos. Chem. Phys. Discuss.*, **4**, 39–69.

Rendtel J. (2004). "Evolution of the Geminids observed over 60 years". *Earth, Moon, and Planets*, **95**, 27–32. https://doi.org/10.1007/s11038-004-6958-5.

Ryabova G. O. and Rendtel J. (2018). "Increasing Geminid meteor shower activity". *MNRASL*, **475**, L77–L80. https://doi.org/10.1093/mnrasl/slx205.

She C. Y., Latifi H., Yu J. R., Alvarez R. J., Bills R. E., and Gardner C. S. (1990). "Two-frequency lidar technique for mesospheric Na temperature measurements". *Geophys. Res. Lett.*, **17**, 929–932.

Uchiumi M., Nagasawa C., Hirono M., Fujiwara M., and Maeda M. (1993). "Sporadic enhancement of the mesospheric sodium during the Perseids meteor shower". *J. Geomag. Geoelectr.*, **45**, 393–402.

Uchiyama S. (2010). "Geminids ZHR activity profiles as a function of magnitude". *WGN, Journal of the IMO*, **38**, 31–35.

von Zahn U., Gerding M., Hoffner J., McNeil W. J., and Murad E. (1999). "Iron, calcium, and potassium atom densities in the trails of Leonids and other meteors: Strong evidence for differential ablation". *Meteorit. Planet. Sci.*, **34**, 1017–1027.

Handling Editor: Javor Kac

Radio meteors

Meteor velocity derived from head echoes obtained by a single observer using forward scatter from a low powered beacon

Felix Verbelen [1]

Radio observation of forward scattered head echoes by a single observer has proven effective in obtaining a good estimate of the velocities of both shower meteors and of sporadics. The method also allows membership assignment of meteors during simultaneous meteor showers.

Received 2018 November 28

1 Introduction

In a former study (Steyaert et al., 2010) researchers explored a general solution for the calculation of a meteor's velocity and its direction. Their method was based on the simultaneous observations of forward scatter head echoes by multiple observers. The study demonstrated it is certainly possible to obtain good results using the multi-station method but there were several problems associated with the multi-station analysis.

The first problem was the requirement for very precise timing of the specular reflections at each of the multiple ground stations. The second problem was that only a limited number of head echoes were observed simultaneously at the different receiver locations unless the angular spread of the receiving stations, as "seen" from the transmitter beacon, was small.

Due to these problems the multiple station solution produced only a limited number of usable head echoes for analysis.

In order to avoid these limitations we considered the feasibility of using a single receiving station observing head echoes from a single beacon.

Two beacon transmitter sites were used in the study. Both beacons are located in Belgium: the VVS radio beacon on 49.99 MHz which is hosted by AstroLab-IRIS near Ieper and the BRAMS radio beacon on 49.97 MHz at Dourbes. Both beacons emit an unmodulated continuous carrier wave (CW) of 50 and 150 watts respectively and both beacons use a single 2-element crossed Yagi antenna pointing to their zeniths. For more info see `http://brams.aeronomie.be/dourbes_beacon`.

For this study, the single receiving station was located in Kampenhout, Belgium. The station was equipped with a 2-element HB9CV antenna pointing to Ieper and with a 3-element Yagi antenna pointing to Dourbes. Both antennas were installed some 3 meters above ground level. The receivers used were a Japanese AITEC MRX-50 designed especially for 49.99 MHz (VVS beacon), and an ICOM R-75 for 49.97 MHz (BRAMS beacon). No pre-amplifiers were used between the antennas and the receivers.

[1]Vereniging voor Sterrenkunde and Volkssterrenwacht Mira. Email: `felix.verbelen@skynet.be`

IMO bibcode WGN-472-verbelen-headechoes
NASA-ADS bibcode 2019JIMO...47...49V

2 Method

2.1 Specular reflection

Forward scattering happens when the radio signal emitted by a transmitter (beacon) is specularly reflected towards the receiver by the ionised trail from a meteoroid entering the atmosphere. The specular reflection point occurs mainly in the range of 80 to 110 km above sea level i.e., in the E-layer of the ionosphere. Such a specular reflection implies that the meteor's atmospheric path is tangent to an ellipsoid where the transmitter and receiver are located at the focal points.

2.2 Vertical plane

All other things being equal, meteors with an atmospheric path in the vertical plane defined by the location of the beacon, the receiving station and the specular reflection point, are likely to produce stronger echoes since this reflection path is the shortest path possible. The use of a suitably tilted directional receiving antenna pointing in the direction of the transmitter highly favours the detection of head echoes in that vertical plane.

As an approximation, we will therefore only consider the case where the meteor's path is in the vertical plane passing through the beacon, the receiver and the specular reflection point.

Likewise, taking into account the modest emission power of the beacons, and thus the limited perimeter of good reception (a few hundred kilometres), the Earth's curvature will be disregarded.

2.3 Locating the specular reflection point in the vertical plane

As mentioned above, in order for a specular reflection to be produced, the meteor's path has to be tangent to a specific ellipse which depends on the distance between transmitter (T) and receiver (R) and on the incident angle of the meteor. For echoes belonging to a meteor shower this incident angle corresponds to the elevation of the shower's radiant. For sporadic meteors the incident angle is the direction of the incoming sporadic meteor (Figure 1).

The general expression for an ellipse is

$$a^2y^2 + b^2x^2 - a^2b^2 = 0 \quad (1)$$

where a and b are the shape parameters of the ellipse: the semi-major and semi-minor axes.

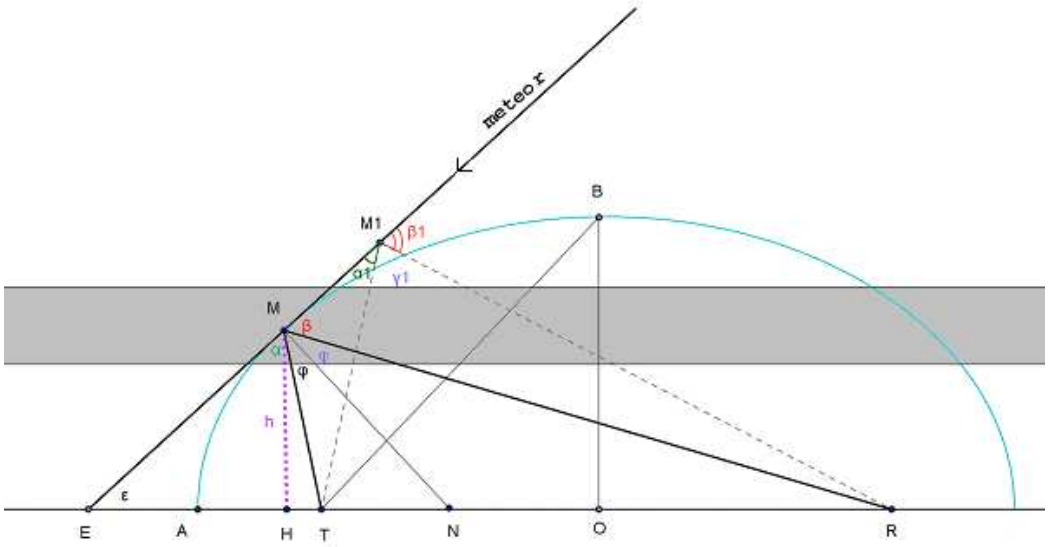

Figure 1 – Graph of the vertical plane including the transmitting beacon (T), the receiving station (R), the position of the meteor at the specular reflection point (M) and at the start of the 1st Fresnel-zone (M1), and the supposed meteor orbit (see text).

The general expression for a tangent to the ellipse is its first derivative:

$$2a^2 y\frac{\mathrm{d}y}{\mathrm{d}x} + 2b^2 x = 0 \qquad (2)$$

Let
TR = the distance between the transmitter and the receiver,
d = TR/2,
h = the height of the specular reflection point in the E-layer, which we know to be at ca. 80 to 110 km,
ε = the elevation of the radiant.

We also know:

$$a^2 = b^2 + d^2$$

and thus,

$$a = \sqrt{(b^2 + d^2)}$$

$$\frac{\mathrm{d}y}{\mathrm{d}x} = \tan(\varepsilon)$$

$$y = h$$

From Equation 1 we deduce that

$$x = \pm a \cdot \sqrt{(b^2 - h^2)}/b$$

and from Equation 2

$$x = -a^2 \cdot h \cdot \tan(\varepsilon)/b^2$$

So we find that

$$h \cdot \tan(\varepsilon) \cdot \sqrt{(b^2 + d^2)} = b \cdot \sqrt{(b^2 - h^2)}$$

This equation can quite easily be solved numerically in order to find b, after giving reasonable values to h (i.e. 90 km) and ε (radiant elevation), d being known.

We thus obtain the ellipse parameters, a and b, corresponding to each set of values attributed to h and ε. By considering a specular reflection point to be at point M (Figure 1), many quantities are also readily obtained.

In Figure 1, where M is the specular reflection point, we find:

OA = TB = a
OB = b
HM = h
OT = OR = d

Setting $y = h$ in Equation 1, and knowing a and b, we find

$x = a \cdot \sqrt{(b^2 - h^2)}/b$; x being OH.

Thus,

$\mathrm{OH} = a \cdot \sqrt{(b^2 - h^2)}/b$
$\mathrm{TH} = \mathrm{OH} - d$
$\mathrm{RH} = \mathrm{OH} + d$
$\mathrm{TM} = \sqrt{(\mathrm{TH}^2 + \mathrm{HM}^2)}$
$\mathrm{RM} = \sqrt{(\mathrm{RH}^2 + \mathrm{HM}^2)}$

The elevations of M at T and at R are respectively
$\angle\mathrm{HTM} = \arctan(\mathrm{HM}/\mathrm{TH})$
$\angle\mathrm{HRM} = \arctan(\mathrm{HM}/\mathrm{RH})$

Knowing TM, RM, and TR and applying the cosine rule, we can find the forward scatter angle TMR:

$$\angle\mathrm{TMR} = \arccos\left(\frac{\mathrm{TM}^2 + \mathrm{RM}^2 - \mathrm{TR}^2}{2 \cdot \mathrm{TM} \cdot \mathrm{RM}}\right)$$

Following the geometrical properties of a tangent to an ellipse, NM, which is by construction perpendicular to the meteor's path at the specular reflection point, divides the forward scatter angle in two equal angles φ:

$\varphi = \angle\mathrm{TMR}/2$

2.4 Elevation of the radiant

It is interesting to note that no, or at the most, very few head echoes are expected if ε is higher than 50–60° above the local horizon.

We know that the meteor's path has to be tangent to the ellipse which is determined not only by the distance

between the transmitter (T) and the receiver (R), but also by the specular reflection point considered to be at a constant height (h) in the E-layer.

If the distance value of TR remains constant, then the half axes a and b of the ellipse will increase as the elevation of the radiant increases. Therefore, the path length of T-M-R (Figure 1) will also increase and due to this increase in path lengths the power received at R will decrease as it is inversely proportional to the square of the total path length.

All other parameters remaining unchanged, i.e. for TR = 100 km and h = 90 km, we can calculate the ellipse parameters and the relative power levels at the receiver when the radiant's elevation increases (Table 1).

McKinley's equation 9-3 (McKinley, 1961:239) leads to similar results as shown in Table 1.

In fact, the received power at the Kampenhout receiver decreases even more quickly than shown in Table 1 since the monitored beacons radiate principally to their zeniths, the beacon's emitted radio power dropping off quite rapidly as the radiation angle decreases.

Therefore, if the elevation of a meteor shower is higher than 60° it is preferable to consider the head echo as being caused by a sporadic, and not by a shower member. For sporadic meteors it is best to assume that its specular reflection point is located at the beacon's zenith, if the beacon emits toward its local zenith, as is the case in our set-up.

The elevation at the receiver of this assumed elevation is readily found:

$$\varepsilon(\text{assumed}) = \frac{\arctan(\text{TR}/h)}{2}$$

The calculated velocity will be somewhat too high if the real elevation of the radiant is lower than the assumed ε, and somewhat lower if the real elevation is higher, but it will nevertheless give a good approximation of the meteor's real velocity.

2.5 1st Fresnel zone

At this point we start taking into account the emission frequency of the beacon.

Let

f_0 = emission frequency at rest.

Thus, the emission wavelength is $\lambda_0 = c/f_0$, c being the speed of light.

If we consider only meteors in the vertical plane trough T and R (see above), then we can modify McKinley's formula 9-2 (Ibid., 238) to find MM_1 (half of the 1st Fresnel zone) as follows:

$$\text{MM}_1 = \sqrt{\frac{\lambda_0 \cdot \text{TM} \cdot \text{RM}}{(\text{TM} + \text{RM}) \cdot (1 - \sin^2(\varphi))}}$$

It follows that

$$\text{TM}_1 = \sqrt{\text{TM}^2 + \text{MM}_1^2 - 2 \cdot \text{TM} \cdot \text{MM}_1 \cdot \cos(\pi/2 + \varphi)}$$

(cosine rule applied to triangle TMM_1)

and

$$\text{RM}_1 = \sqrt{\text{RM}^2 + \text{MM}_1^2 - 2 \cdot \text{RM} \cdot \text{MM}_1 \cdot \cos(\pi/2 - \varphi)}$$

(cosine rule applied to triangle RMM_1).

2.6 Doppler shift in forward scatter

A radio wave emitted by T and reaching a moving meteor will show a Doppler shift of $\Delta f_1 = v/c \cdot f_0 \cdot \cos(\alpha)$ to an observer at M, where α is the angle between the direction of the moving meteor and the direction towards T, and v is the meteor's velocity. In forward scatter, there are two Doppler shifts involved. The radio wave from the transmitter frequency as "seen" by at meteor (M), is $f_1 = f_0 + \Delta f_1$. The signal is again reflected forward from M towards R and so the signal is affected by a second Doppler shift of $\Delta f_2 = v/c \cdot f_1 \cdot \cos(\beta)$, where β is the angle between the direction of the moving meteor and the direction towards R.

Combining both Doppler shifts, we find that a radio wave with frequency f_0 emitted at T is affected at R by a total Doppler shift

$$\Delta f = v/c \cdot f_0 \cdot (\cos(\alpha) + \cos(\beta)) \quad (3)$$

Near the specular reflection point the meteor is approaching T but regressing from R, and so Δf_1 will be positive, while Δf_2 will be negative. Therefore we can transform Equation 3 as follows:

$$\Delta f = v/c \cdot f_0 \cdot (\cos(\alpha) - \cos(\beta)) \quad (4)$$

At the specular reflection point $\alpha = \beta$, and thus, $\Delta f = 0$ when the meteor is at that point.

At any other point of the meteor's atmospheric path, $\Delta f \neq 0$. This is for example the case at M_1, the beginning of the 1st Fresnel zone, where $\alpha_1 \neq \beta_1$ (Figure 1).

Solving for α_1, γ_1, β_1:

$$\alpha_1 = \arccos\left(\frac{\text{MM}_1^2 + \text{TM}_1^2 - \text{TM}^2}{2 \cdot \text{MM}_1 \cdot \text{TM}_1}\right)$$

(cosine rule applied to triangle MM_1T)

$$\gamma_1 = \arccos\left(\frac{\text{TM}_1^2 + \text{RM}_1^2 - \text{TR}^2}{2 \cdot \text{TM}_1 \cdot \text{RM}_1}\right)$$

(cosine rule applied to triangle TM_1R)

$$\beta_1 = \pi - \alpha_1 - \gamma_1$$

2.7 Head Echoes

Using the forward scatter single receiver set-up, briefly described earlier, a number of measurable head echoes were obtained each day. This number increased dramatically during major meteor showers.

Figure 2 shows a typical strong head echo obtained on 2018 June 07, at $06^{\text{h}}19^{\text{m}}$ UT at the Kampenhout receiver site. The x-axis of the image has a 2 seconds timespan while the y-axis spans a frequency interval of 1000 Hertz.

Considering the relatively small time interval, the change in frequency can, as a first approximation, be considered as being linear. We can then schematically represent the head echo as shown in Figure 3.

The main characteristics of the head echo are obtained by determining the values of freq_1 and freq_2 and of t_1 and t_2.

Table 1 – Received power percentages of head echoes vs. an increase in the radiant's elevation.

Elevation radiant (°)	a (km)	b (km)	Path T-M-R (km)	Power received (%)
0	103	90	206	100
10	105	92	209	97
20	109	97	219	89
30	118	107	236	76
40	131	122	263	61
50	153	145	306	45
60	192	185	383	29
70	272	267	544	14
80	523	521	1046	4
90	∞	∞	∞	0

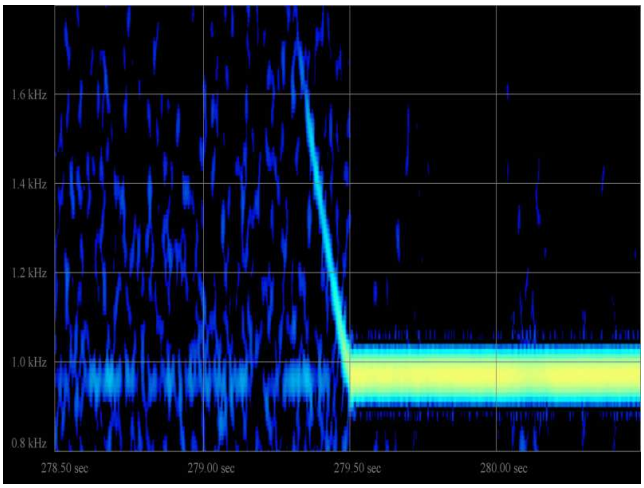

Figure 2 – Typical echo obtained on 49.99 MHz.

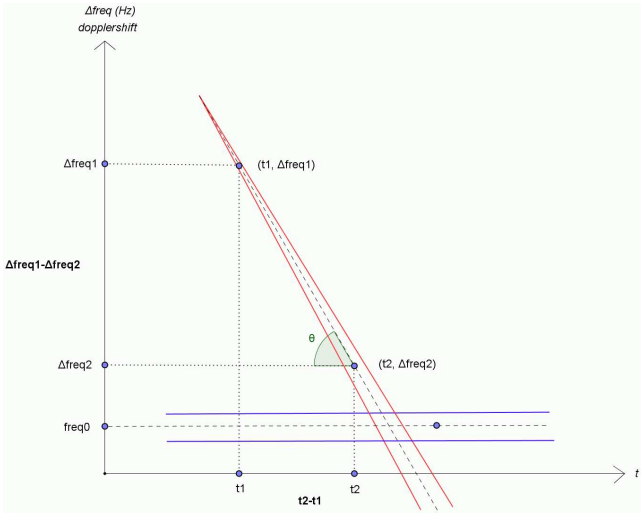

Figure 3 – Schematic head echo, with the frequencies and time instants to measure.

Measuring the head echo we obtain

$$\tan(\theta) = \frac{\text{freq}_2 - \text{freq}_1}{t_2 - t_1}$$

$\tan(\theta)$ is also called the "slope" of the head echo.

By measuring Δfreq_0 we can quite accurately determine the instant the head echo reaches the specular reflection point.

Considering the meteor's velocity as constant throughout the 1st Fresnel zone as well as during the time interval $(t_1 - t_2)$ of the head echo, we find the meteor's velocity in the 1st Fresnel zone as:

Let Δt_z = time needed to cross the 1st Fresnel zone

Δf_z = frequency change while crossing the 1st Fresnel zone.

Thus, $v = \text{MM}_1/\Delta t_z$

Since we assumed that the slope, $\tan(\theta) = \Delta f_z/\Delta t_z$ we know that:

$v = \text{MM}_1 \cdot \tan(\theta)/\Delta f_z$

or

$\Delta f_z = \text{MM}_1 \cdot \tan(\theta)/v$

From Equation 4 we know that

$\Delta f_z = v \cdot f_0 \cdot (\cos(\alpha_1) - \cos(\beta_1))/c$

Therefore we can directly obtain the meteor's velocity in the vicinity of the specular reflection point as:

$$v = \sqrt{\frac{c \cdot \text{MM}_1 \cdot \tan(\theta)}{f_0 \cdot (\cos(\alpha_1) - \cos(\beta_1))}}$$

Pierre Ernotte (Ernotte, 2018) has shown that this can also be written as: $v = \text{MM}_1 \cdot \sqrt{(-\Delta f_z/\Delta t_z)}$

3 Results

In order to test our calculation method, the velocities of head echoes were derived as proposed during several major meteor showers. The echoes were recorded at Kampenhout from both the VVS beacon near Ieper where $f_0 = 49.99$ MHz at a distance of TR = 120 km, and from the BRAMS beacon at Dourbes where $f_0 = 49.97$ MHz at a distance of TR = 94 km.

3.1 Quadrantids 2018 on 49.99 MHz (VVS beacon near Ieper)

The slopes of all measurable head echoes during the period of 2018 January 3, $00^{\text{h}}00^{\text{m}}$ UT and 2018 January 4, $24^{\text{h}}00^{\text{m}}$ UT were determined. All of these head echoes were assumed to belong to the Quadrantids shower and therefore, the local elevation of the Quadrantids radiant at the time of the head echo was used.

A total of 71 Quadrantids head echoes were measured.

Assuming an ionisation height of 90 km, a clear peak showing a typical shower velocity of 42 km/s was seen (Figure 4). In comparison, the IMO's 2018 Meteor Shower Calendar (Rendtel, 2017) shows a velocity of

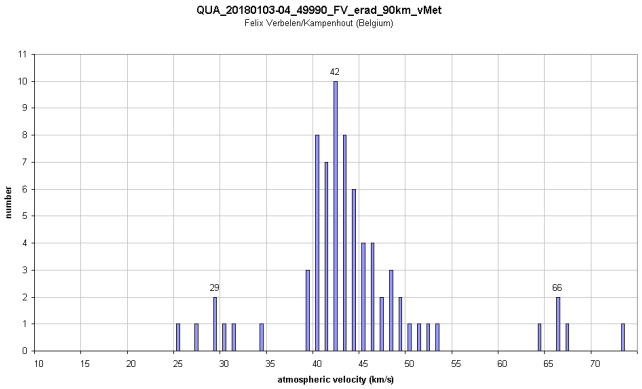

Figure 4 – Velocities (km/s) derived from head echoes on 2018 January 03–04. Apart from the Quadrantids with typical velocities of 42 km/s, other showers with meteor velocities around 29 and 66 km/s seem to be active.

41 km/s for this shower, while the IAU MDC lists a range of velocities between 40.0 and 42.0 km/s (Jopek & Kanuchova, 2017).

As seen in Figure 4, during the same time period several minor showers seem to be occurring with their velocities clustering around 29 km/s and at 66 km/s. Since the velocities were calculated taking into account the radiant elevation of the Quadrantids, the "secondary peaks" are also to be considered a preliminary approximation.

3.2 Geminids 2017 on 49.99 MHz (VVS beacon near Ieper)

A total of 191 head echoes were measured between 2017 December 12, $00^{h}00^{m}$ UT and 2017 December 14, $24^{h}00^{m}$ UT. The local radiant's elevation of the Geminids were adopted for all the measured head echoes.

The ionisation height was again presumed to be at 90 km. A clear peak was found, with 35 meteors showing a typical shower velocity of 36 km/s (Figure 5). The IMO's 2018 Meteor Shower Calendar, op. cit., lists a velocity of 35 km/s for this shower, while the IAU MDC, op. cit., shows a range between 34.6 and 35.0 km/s.

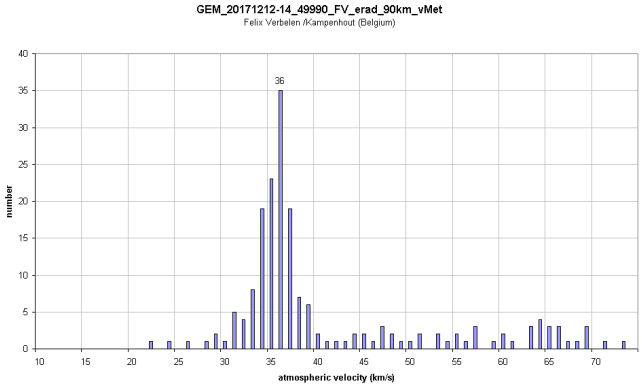

Figure 5 – Velocities (km/s) derived from head echoes on 2017 December 12–14. The Geminids show typical velocities of 36 km/s.

3.3 Perseids 2011 on 49.97 MHz (BRAMS-beacon at Dourbes)

For this shower the head echoes were measured between 2011 August 12, $00^{h}00^{m}$ UT and 2011 August 15, $24^{h}00^{m}$ UT. Note that unlike the other showers where $h = 90$ km, an ionisation height of 100 km was assumed for this shower. This was done because several authors cf. i.e. Greenhow J.S. and Hall J.E. (1960) have long pointed out that the ionisation height increases with higher meteor velocities.

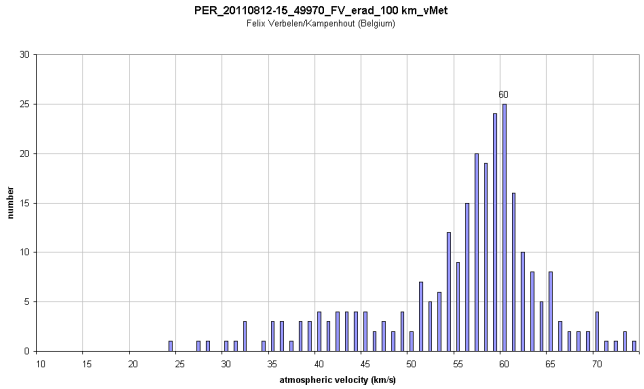

Figure 6 – Velocities (km/s) derived from head echoes on 2011 August 12–15. The Perseids show typical velocities of 60 km/s.

A total of 271 head echoes were measured during the period mentioned above. All of these head echoes were assumed to belong to the Perseids shower and so the local radiant's elevation of the shower was adopted for all the measured head echoes.

Once again, a clear peak of 25 meteors occurred at 60 km/s which is a typical velocity for a Perseid member (Figure 6). In comparison the IMO's 2018 Meteor Shower Calendar, op. cit., lists a velocity of 59 km/s, while the IAU MDC, op. cit., lists a range between 58.7 and 62.1 km/s for Perseids members.

Obviously not all the head echoes originated solely from the Perseids; other minor showers were active during the Perseids, as were sporadics. As a result of assuming the local radiant elevation of the Perseids for all the head echoes sampled, some of the derived velocities were biased which explains the calculated velocities greater than 72 km/s.

The same remark is valid for the other shower examples. As explained earlier, if the shower local radiant elevation is higher than 60 degrees above the horizon, then it is preferable to attribute the head echoes as being caused by sporadics meteors and not by a shower's member.

4 Conclusion

Using a single forward scatter receiver as described above and knowing only:

- the distance (TR) between transmitter and receiver,
- the beacon's frequency (f_0),

- the "slope" of the head echo ($\tan(\theta)$), and, if possible,
- the radiant's elevation (ε)

and assuming a reasonable ionisation height (h), it is possible to calculate the meteor's velocity in the immediate vicinity of the specular reflection point.

Neglecting the azimuth of the radiant, as in our approach, does not seem to have a major impact on the results as the many comparisons with velocities derived by other methods (visual, photographic and radar) have shown.

Our method can certainly be refined, but in its current state it seems to quickly provide reliable results for determining a head echo's velocity and whether the meteor is a member of a particular shower or not. It also eliminates the low samples sizes and the critical requirement for precise timing that occurs in the multiple stations method.

Acknowledgements

The author is particularly indebted to Pierre Ernotte, Christian Steyaert and Jeffrey Brower for many helpful discussions and proof-reading this paper, and to Dirk Van Hessche, Willy Camps, Lucas Pellens, Joseph Welkenhuyzen and many others for sharing their radio observations.

References

Ernotte P. (2018). "Forward scattering: an interesting formula to calculate the velocity of a meteoroid that generates a head echo". *WGN, Journal of the IMO*, **46:6**, 198–200.

Greenhow J. S. and Hall J. E. (1960). "The variation of meteor heights with velocity and magnitude". *MNRAS*, **121**, 174–182.

Jopek T. J. and Kanuchova Z. (2017). "List of all meteor showers, IAU Meteor Data Center". `https://www.ta3.sk/IAUC22DB/MDC2007/Roje/roje_lista.php?corobic_roje=0&sort_roje=0`.

McKinley D. W. R. (1961). *Meteor Science and Engineering*. McGraw-Hill Book Company, Inc, Toronto.

Rendtel J. (2017). "2018 Meteor Shower Calendar". Potsdam. IMO_INFO (2-17); `https://www.imo.net/files/meteor-shower/cal2018.pdf`.

Steyaert C., Verbelen F., and de VVS Beacon Observers (2010). "Meteor Trajectory from Multiple Station Head Echo Doppler Observations". *WGN, Journal of the IMO*, **38:4**, 123–129. `http://cdsads.u-strasbg.fr/abs/2010JIMO...38..123S`.

Handling Editor: Jean-Louis Rault

Automated Spectrogram Analysis for Meteor Head Echoes

C. Powell[1]

The Meteor Echo Spectrogram Analysis (MESA) program is developed to automatically identify meteor head echoes in spectrograms generated by forward-scatter radio meteor detection. The program is both extensible and flexible, allowing calculations such as line-of-sight approach and recede velocities, duration, and maximum intensity. A detection sensitivity of 0.790 is achieved, with an improved sensitivity of 0.875 when only low-noise spectrograms ($\sim \frac{2}{3}$ of the data) are analysed. The MESA program cannot fully replace manual analysis of spectrograms, but greatly reduces the volume of data that needs processing.

Received 2019 February 9

1 Introduction

The aim is to produce a computer program that takes spectrogram images generated by forward-scatter radio meteor detection as input, and identifies meteor head echoes in the spectrogram. The program may also make an estimate of the approach & recede velocity, maximum intensity, start time, end time, and duration, of each identified meteor echo.

The computer application uses a number of image processing techniques applied in a manner motivated by the characteristic shape of meteor echoes in spectrograms, to identify the 'centre' of each echo based on a centre of mass algorithm, which uses RGB pixel values as weights. Velocities may then be estimated using the Doppler equation and identification of the 'start' and 'end' of each echo, again using image processing techniques.

In order to verify the accuracy of the program, results are compared to manual calculations of a random selection of data over a timespan of 1 week to determine the sensitivity of the program.

As with all methods of visualising data, spectrograms lose some of the original data (i.e. the radio signal from detection is not kept). However, spectrograms are often the only practical way that data can be archived for an observer - no 'level 1' data is available, so automated spectrogram analysis is a useful tool.

2 Background

The theory behind forward-scatter radio meteor detection and the resulting meteor echo characteristics in spectrograms is discussed, as well as necessary theory for velocity estimation, and past work to identify meteor echoes in spectrograms.

2.1 Spectrogram generation

Detecting meteors using forward-scatter radio uses a transmitter broadcasting over a wide area of sky, through which meteors pass. The ionised trail of a meteor reflects the radio signal, which can then be picked up by a receiving station.

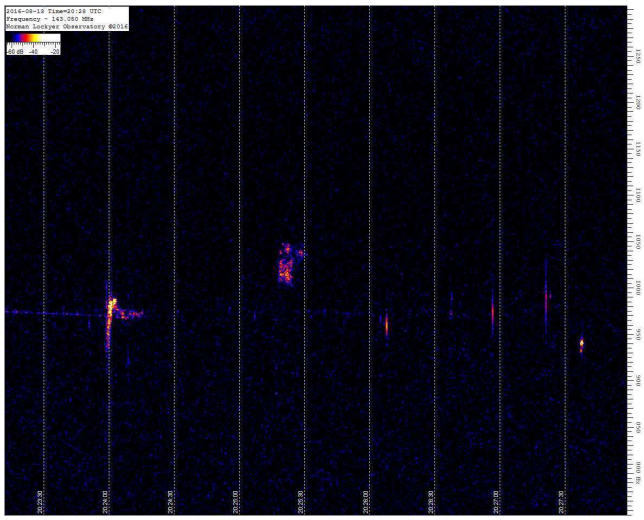

Figure 1 – Spectrogram generated by Spectrum Lab v3.0

Programs such as Spectrum Lab [a] receive the signal generated by radio detection and produce spectrograms (Figure 1), which are three-dimensional representations of the data: the horizontal axis is time, the vertical axis is (modulated) frequency, and the third axis is signal intensity, represented using a colour scale. Often the CMRmap colour scale is used (Figure 2). Spectrograms are sometimes referred to as 'waterfall' plots.

Figure 2 – CMRmap colour scale

Spectrograms most often cover a 5-minute interval, so a single detection station may generate 288 spectrograms per day: manual analysis of this is not practical, hence automated analysis is necessary.

2.2 Meteor echo characteristics

Assuming upper sideband forward-scatter radio detection is used, and the spectrogram uses a CMR colour scale, meteor echoes appear as white (high intensity) vertical streaks, often with highest intensity close to the carrier wave (CW) frequency. Note that often the

[1]Email: cpowell@cwp.io

IMO bibcode WGN-472-powell-spectrogram
NASA-ADS bibcode 2019JIMO...47...55P

[a]Available at http://www.qsl.net/dl4yhf/spectra1.html

CW frequency is demodulated and shifted, so that the direct signal, when visible, does not appear in the spectrogram at the transmitted CW frequency.

The CW frequency corresponds to zero line-of-sight (LOS) velocity of the meteor. Greater frequencies than CW correspond to greater LOS approach velocity, and lower frequencies than CW correspond to greater LOS recede velocity. Velocity can be (naïvely) calculated using the Doppler equation

$$\frac{\Delta f}{f} = \frac{v}{c} \tag{1}$$

where c is the speed of light in a vacuum. This assumes a simple structured echo; more complex echoes require more detailed techniques for velocity estimation. Note also that the Doppler shift is in fact made up of two parts; a shift owing to the radial velocity between the meteor and transmitting station, and a shift owing to the radial velocity between the meteor and receiving station. Only the Doppler shift of the former radial velocity is considered, limiting the accuracy of the velocity estimate.

Some radar systems receive a direct signal from the transmitter, meaning the CW frequency (after shifting/demodulating) is immediately obvious. For other systems the resultant CW frequency may be determined by averaging many images together until the direct signal is apparent.

2.3 Past work

Echo-counting software has been developed before, for example Noguchi & Yamamoto (2008) developed an image processing tool to automatically analyse HROFFT spectrograms however no capacity for further calculations is included. A 90% agreement between manual and automatic counting was found. Artificial Neural Networks have also been used to attempt to automatically identify echoes in spectrograms (Roman & Buiu, 2015).

3 Design

An example spectrogram (Figure 1) is used to show each step of the processing & analysis.

3.1 Data assumptions

The MESA program assumes that data is provided with a size of 800 × 1133 pixels, and the CMRmap colour scale is used, with a detection setup using upper-sideband forward-scatter radio detection. However, settings can be modified to remove these assumptions and allow use of any colour scale and image dimensions necessary. Namely, the number of pixels to be removed on each edge (to remove elements such as the legend and frequency scale), and the RGB channel to be extracted. The program may also be modified to use lower-sideband radio detection.

3.2 Data pipeline

It is envisaged that the automated echo detection system is part of a more complex data pipeline where large, high-quality images are passed to this automated detection system where they are processed and subsequently saved to an archive in a lower quality format to reduce the necessary amount of memory storage. This removes issues raised by compression artefacts, for example in JPEG compression (Figure 3). If lossless compression is used prior to processing, this pipeline is not necessarily needed.

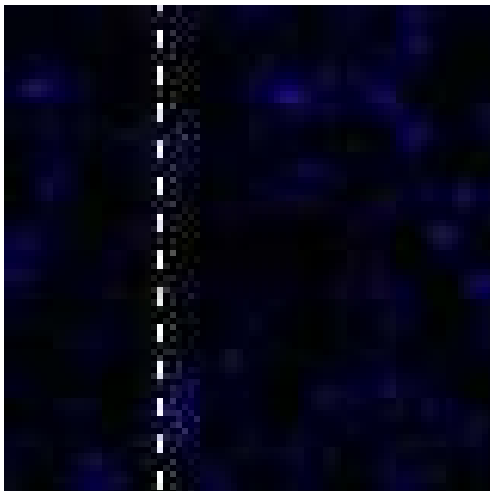

Figure 3 – JPEG compression artefacts

3.3 Pre-processing

Irrelevant data must be removed from the image to aid the analysis, namely the colour scale, legend, frequency scale, and timestamps. The user must enter a depth in pixels for each border of the image so that these can be removed. Spectrograms produced by Spectrum Lab also have vertical dashed bars indicating 30 second time increments, which must be removed. Since use of the CMRmap colour scale is assumed, only the red RGB channel is extracted from the image. The blue and green channels hold redundant data: most noise appears blue, whilst echoes are red to white. The image is also stretched with horizontal scale-factor 3, for reasons discussed in Section 3.5, producing Figure 4.

The colour scale must also be identified within the image to allow calculation of maximum intensity for each meteor echo.

3.4 Denoising

Before echoes can be identified in the image, noise must be removed. There is often a large amount of noise throughout the image, as can be seen from the blue spots in Figure 1. The denoising process uses thresholding, erosion, a total variation filter, and dilation.

The image is first dynamically thresholded using the Otsu method (Otsu, 1979). This is a common first step in image segmentation algorithms, and is a clustering-based threshold method which minimises the intra-class variance of the image's gray-level histogram, splitting the image into 'foreground' and 'background'. The background is removed by replacing every 'background' pixel with value 0. The result is an image with significantly reduced noise, Figure 5.

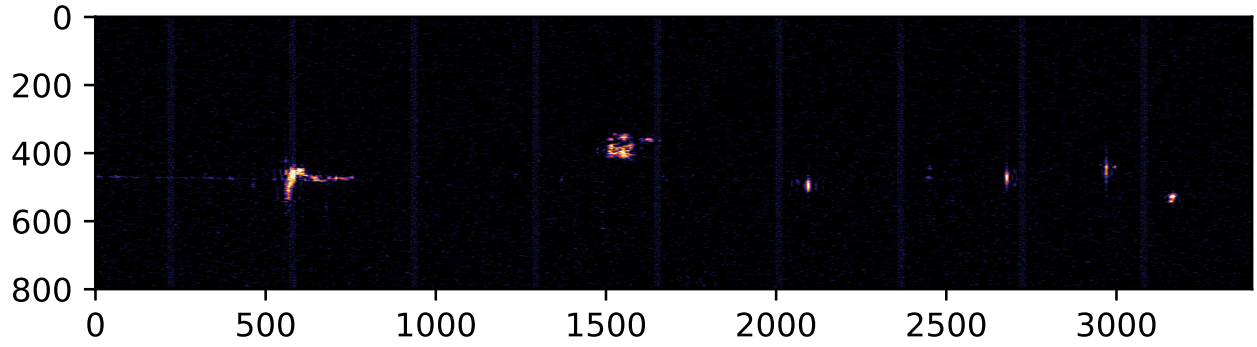

Figure 4 – Spectrogram after pre-processing.

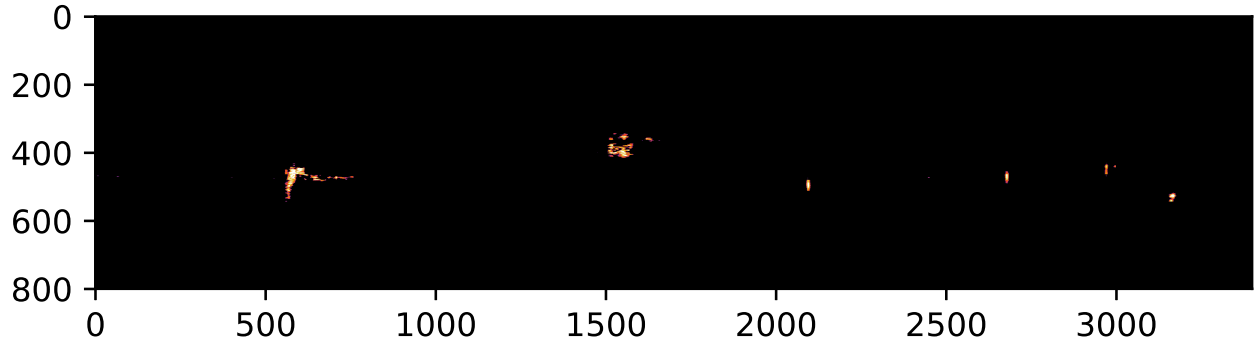

Figure 5 – Spectrogram after thresholding.

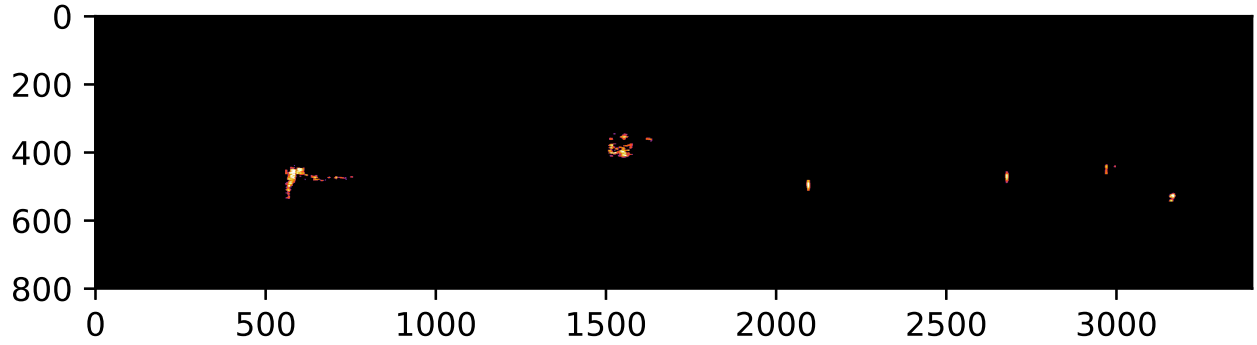

Figure 6 – Spectrogram after erosion, denoising, and dilation.

Erosion and dilation filters (Gonzalez & Woods, 2002) set each pixel to the minimum and maximum (respectively) over all pixels in a neighbourhood centred at the given pixel. Erosion filters shrink bright regions and enlarge dark regions, whilst dilation filters do the opposite. Erosion often breaks up regions and removes low-σ noise (large signal-to-noise ratio), whilst dilation rejoins broken regions. A combination of the two, with a denoising filter in between, allows shapes to be smoothed, broken regions reconnected, and remaining noise removed (Figure 6).

A total-variation Chambolle denoising filter (Chambolle, 2004) is used due to its property of preserving edges whilst smoothing noise in flat regions, even with low signal-to-noise ratios.

3.5 Echo identification

Owing to the characteristic shape of meteor echoes as streaks, a kernel convolution (with kernel in Figure 7) replicating this shape is used to identify regions of the image that may contain echoes. A large kernel is used since echoes are large relative to the image dimensions (800 by 1133 for comparison data), on the order of 40 pixels in height and 10 pixels in width, at minimum. This is a common image processing technique, though is often only part of a more complex algorithm (Šustr, 2013). It is advantageous to use this method before region identification since artefacts may remain in the image after denoising, whether due to radio effects such as tropospheric propagation and interference, or artefacts of the prior processing, and these are often dissimilar to

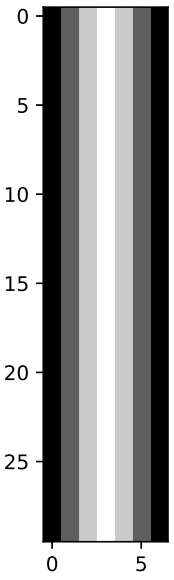

Figure 7 – Normalised kernel used for streak convolution.

the echoes in shape, so are easily removed (or at least nullified) with a streak convolution (see Figure 8).

Region identification is performed using connected-component analysis (CCA) (Dillencourt et al., 1992). This is a method of labelling image pixels based on connected components satisfying a given heuristic. Many algorithms exist and choice depends on convenience, availability for implementation in a given language, and speed. 4-connectivity is used in the interest of processing speed, since echo shapes are assumed to be basic and do not require 8-connectivity. Once regions are labelled, centres of mass are calculated with the R component of pixel RGB values as weights. This provides an approximate location for the centre of the echo. These centres are marked with crosses in the final results (Figure 5.1). This process gives Figure 9.

The dilation filter in the denoising process does not always reconnect broken regions, so sometimes echoes may still be split in two after this filter is applied. Similarly, the appearance of an echo in the spectrogram may simply be split on detection (see Figure 10). Thus, once images have been split into regions, these regions must be rejoined. This is done by identifying any region that overlaps horizontally with another region. These are then recategorised as the same region. Note that vertical overlapping is not considered since the time axis is horizontal, so horizontally distinct regions occur at distinct times and should not be considered the same echo. Despite this, some echoes occur so close in time that they overlap slightly. In order to separate these echoes the image is stretched horizontally, giving greater resolution in time.

In some spectrograms erroneous detections occur, primarily due to radio artefacts, and these can be identified from their vertical position: the majority of echoes are underdense which have their centre of mass close to the CW frequency, so by considering vertical locations outliers can be removed. The definition of an outlier as beyond 1.5× the inter-quartile range of the vertical centre of mass locations is used, which is calculated on a per-image basis.

3.6 Calculations

In order to calculate the start and end time of a given echo, the horizontal location (in pixels) of the echo region bounding box is used, as well as a user-specified seconds-per-pixel value and the image's timestamp. Duration is then easily calculated from the start and end times, which are given in the timezone the original spectrogram uses (usually UTC).

The top and bottom locations of the echo region bounding box are used to estimate approach and recede velocities using the Doppler equation (1), which requires a user-specified Hz-per-pixel value and the demodulated CW frequency vertical location in the image, specified in pixels. Results are given in kilometres per second.

Maximum intensity is calculated by identifying the pixel in a given echo region with the greatest value relative to the colour scale in the image, which requires the user to locate the scale within the image during the pre-processing stage.

An overview of the design of the MESA (meteor echo spectrogram analysis) program is given in Figure 11.

4 Implementation details

The program is written in Python 3 (available at `www.python.org`).

4.1 Libraries

Libraries used are:

- NumPy (available at `www.numpy.org`) is a module used for computation throughout the program since it is optimised for vectorised data, so is efficient for working with images when represented as arrays.
- Matplotlib (available at `matplotlib.org`) is a plotting tool used to display the spectrogram and graphics associated with analysis, such as circling the estimated echo centres.
- OpenCV (available at `docs.opencv.org/3.0-beta/modules/core/doc/intro.html`) is a computer vision module used for common image processing techniques such as denoising, erosion filters, and dilation filters.
- SciPy (available at `www.scipy.org`) is a scientific computing library used here for connected-component analysis.
- Scikit-Image (available at `scikit-image.org`) is an image processing library providing efficient implementations of Otsu thresholding and TV Chambolle denoising.

4.2 Pseudocode

Pseudocode for important processes in the program are shown in appendices B, C, and A, namely rejoining of broken echoes, estimation of max intensity for a given

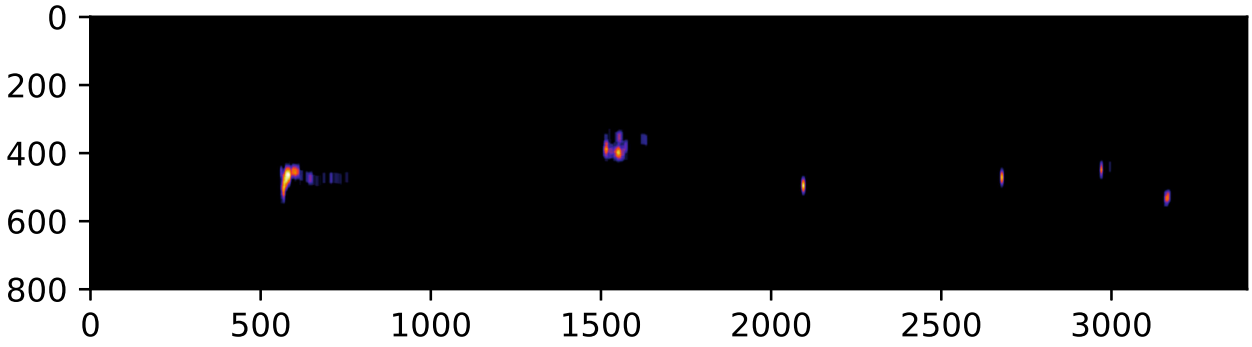

Figure 8 – Spectrogram after thresholding.

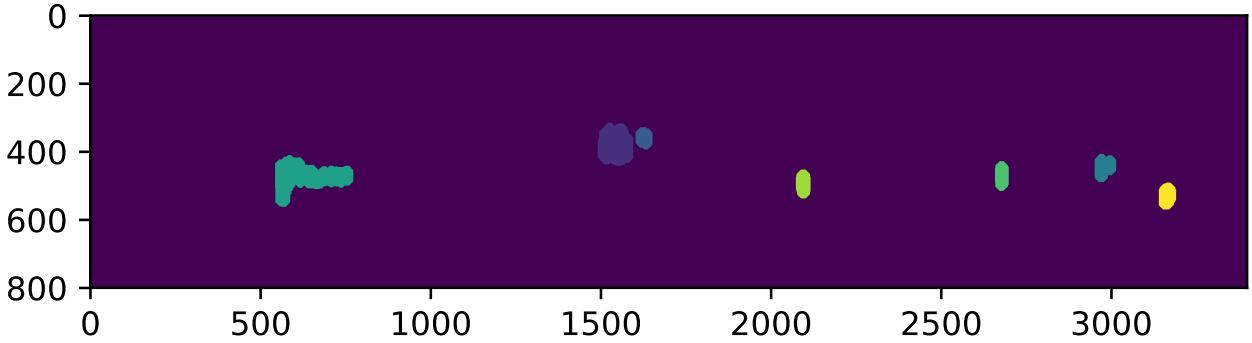

Figure 9 – Spectrogram after region labelling.

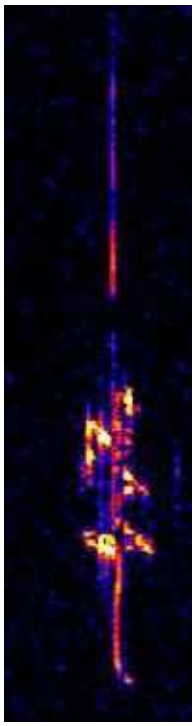

Figure 10 – Some echoes may be split vertically.

list of echo centre-of-masses, and removal of lines in pre-processing. Variables defined earlier in the program are underlined (and thus passed as an argument to the function if needed).

Algorithm 1 in appendix A shows the process for removing the vertical lines which indicate 30 second increments in the spectrogram. The mean RGB value of the bottom pixel of each line is checked and the greatest 9 are chosen (assuming there are 9 lines). The bottom pixel is checked since in the images the lowest pixel is where the bar starts, so is white, thus the mean RGB value of this pixel is approximately 255.

Algorithm 2 in appendix B shows the process for reconnecting broken echo regions. A vertical column strictly containing the given echo region is checked for other regions. Those identified are recategorised as part of the original region.

Algorithm 3 in appendix C is used to estimate the maximum intensity of a given detected echo. Each pixel in the region has its maximum intensity calculated: first the index is found for the part of the colour scale with the minimum colour difference, then linear interpolation between the corresponding intensity at the start and end of the scale gives the pixel's intensity. The maximum of these intensities and the corresponding pixel is then identified.

4.3 Calculations

Formulae for the various calculations are shown below using variables entered by the user (in **bold**), or calculated previously in the program (in *italics*).

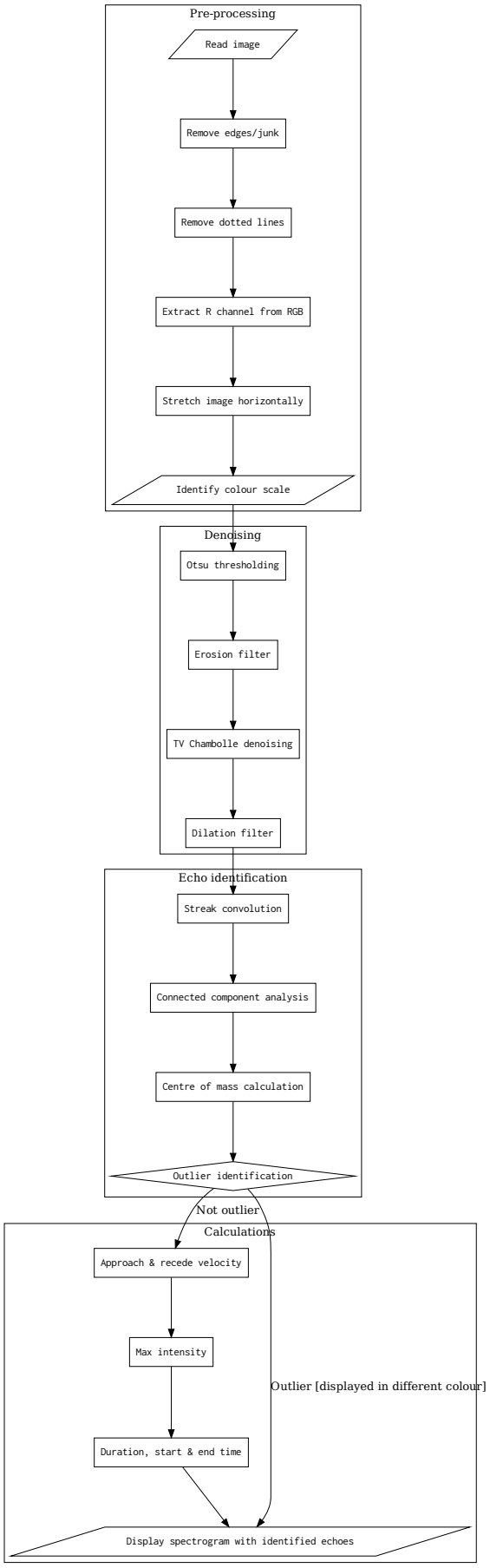

Figure 11 – Flowchart of MESA program.

Approach & recede velocity

$$\begin{aligned} f_{\text{rec}} &= (\mathit{bottom} - \mathbf{CWfreq}) \cdot \mathbf{HzPerPixel} \\ f_{\text{appr}} &= (\mathbf{CWfreq} - \mathit{top}) \cdot \mathbf{HzPerPixel} \\ v_{\text{rec}} &= \frac{c \cdot f_{\text{rec}}}{\boldsymbol{f}_{\mathbf{CW}}} \\ v_{\text{appr}} &= \frac{c \cdot f_{\text{appr}}}{\boldsymbol{f}_{\mathbf{CW}}} \end{aligned} \tag{2}$$

where *bottom* is the distance in pixels between the bottom of the echo region and the top edge of the image; *top* is defined similarly, **CWfreq** is the vertical location (in pixels) of the CW frequency in the spectrogram, **HzPerPixel** indicates Hz per vertical pixel, c is the speed of light in a vacuum, given in $km \cdot s^{-1}$. Results are given to an accuracy of 3dp.

Max intensity

$$I_{\text{dB}} = \frac{\boldsymbol{i}}{\boldsymbol{l}} \cdot (\boldsymbol{s}_{\mathbf{min}} - \boldsymbol{s}_{\mathbf{max}}) - \boldsymbol{s}_{\mathbf{offset}} \tag{3}$$

where $\boldsymbol{i}$ is the index of the colour scale pixel with the minimum colour difference to the current pixel, and $\boldsymbol{l}$ is the length of the colour scale in pixels. $\boldsymbol{s}_{\mathbf{max}}$, $\boldsymbol{s}_{\mathbf{min}}$ are the maximum and minimum intensities on the scale when offset by $\boldsymbol{s}_{\mathbf{offset}}$ so that $\boldsymbol{s}_{\mathbf{min}}$ is 0. This variable, despite always being 0, is kept to aid clarity.

Start & end time

$$\begin{aligned} \Delta t_{\text{start}} &= \mathbf{sPerPixel} \cdot \left[w_{\text{image}} - \left(\mathit{left} + n^{l}_{\text{lines}} \right) \right] \\ t_{\text{start}} &= t_{\text{image}} - \Delta t_{\text{start}} \\ \Delta t_{\text{end}} &= \mathbf{sPerPixel} \cdot \left[w_{\text{image}} - (\mathit{right} + n^{r}_{\text{lines}}) \right] \\ t_{\text{end}} &= t_{\text{image}} - \Delta t_{\text{end}} \end{aligned} \tag{4}$$

where **sPerPixel** identifies the number of seconds per horizontal pixel, w_{image} is the width of the image, *right* is the distance in pixels of the right side of the echo region (where the left edge of the image is 0 and the right edge of the image is w_{image}), *left* is defined similarly, $n^{l,r}_{\text{lines}}$ is the number of lines removed between the left edge of the image and the left (or right) edge of the echo region, used to adjust the time based on how many pixels were removed in preprocessing.

5 Comparison

To test the performance of the MESA program, the sensitivity was calculated from a set of spectrograms analysed both manually and automatically. The equivalent of one day of data was analysed. Since each spectrogram covers 5 minutes, 288 images must be processed: first, every fifth spectrogram is selected from a week of data 15th August 2016 to 21st August 2016, inclusive, from which a random sample of 288 images was taken. A short timescale was used so that changes in the detection setup and spectrogram generation, such as the colour scale parameters, are unlikely to have occurred.

The performance of the MESA program was then analysed by manually processing the 288 images with

the program results overlaid and recording the number of true positives (successful detections), false positives (non-head echo detections), and false negatives (missed head echoes). This indicates the proportion of detections that are actually head echoes, and how often head echoes are missed. In order to test the performance of the program relative to how noisy the spectrogram is, the mean-squared error (MSE) of the pixel values was calculated as a measure of noise, so that the relationship with sensitivity can be seen. The sensitivity of the MESA program was then determined as the average proportion of true positives per spectrogram out of the true positives and false negatives for the same spectrogram. The sensitivity was then calculated for spectrograms with MSE below a given threshold and plotted against these thresholds, which ranged from 50 to 120. A histogram of the MSE noise is shown in Figure 12.

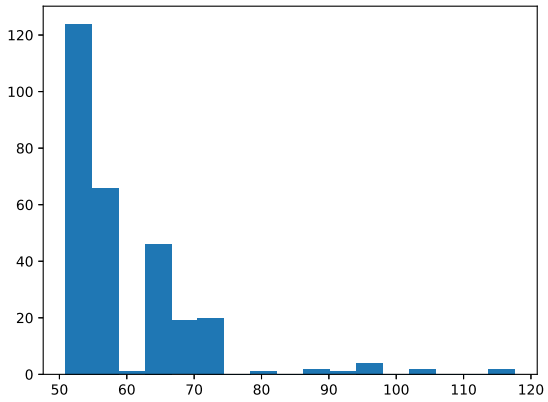

Figure 12 – Histogram of mean-squared error noise of the spectrogram data.

No analysis was made of the accuracy of regions identified around each head echo: the choice of bounding region is largely subjective and it would be almost impossible to quantify the performance of the program. The important aspect of the program is that it functions consistently, considering one of the purposes of automated analysis is to give an objective way to identify echo regions to allow comparison of different sets of data, whilst manual analyses by two different persons may disagree.

5.1 Results

Performance analysis In the 288 images there are in total 1048 successful detections, 1244 false detections, and 255 missed detections, resulting in a per-spectrogram average of 3.64 successful detections, 4.32 false detections, and 0.89 missed detections.

This shows that 54% of detections are not actually head echoes. However, 69% of spectrograms have no missed detections, and excluding blank spectrograms (that is, no successful, false, or missed detections) then 87% of spectrograms have no missed detections.

The sensitivity of the program has a clear inverse relationship with the MSE of the image being processed:

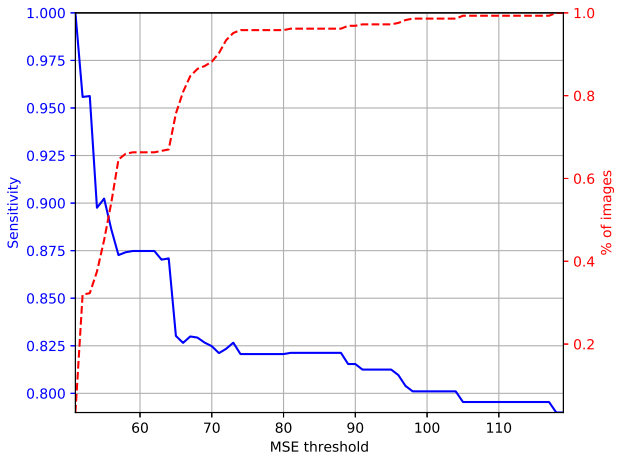

Figure 13 – Sensitivity against MSE threshold, with percentage of images with MSE less than the threshold.

see Figure 13. Including all spectrograms, the sensitivity of the program is 0.790. Including spectrograms only with MSE noise < 60, which accounts for $\sim 65\%$ of the spectrograms, the sensitivity of the program rises to 0.875.

Example spectrograms Certain artefacts in spectrograms result in poor performance of the MESA program, for example high noise (Figure 14b), direct signals and aeroplanes (Figure 14c), and tropospheric propagation (Figure 14d). An ideal spectrogram is shown in Figure 14a.

6 Discussion

6.1 MESA performance

These results show that whilst a large proportion of the programs detections are not head echoes, relatively few head echoes are missed. The program performs well on spectrograms with low noise (MSE < 60): these are most commonly spectrograms without direct signal and other artefacts. Large amounts of noise (specifically signal-to-noise ratio) means the program cannot distinguish between echoes and noise. Thus different types of noise or artefacts impede the program in different ways. When the noise arises as 'blobs', the streak convolution removes this. If the noise arises as streaks, for example when aeroplanes have been detected (in which case there are effectively multiple very short streaks next to each other), the streak convolution doesn't remove the noise and the program performs poorly. This also occurs when there is a direct signal. When the colour scale is not calibrated to eliminate noise, the denoising process it not capable of removing it.

The results demonstrate that the MESA program does not perfectly replace manual processing, however it allows significant reduction in the volume of data that must be manually processed.

6.2 Limitations

Available data Only 50% quality JPEG spectrograms were available for the analysis of MESA performance, whilst the program is envisaged for use with

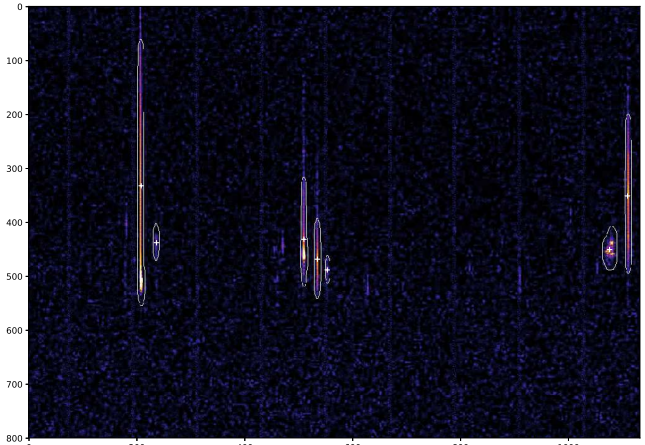

(a) The ideal spectrogram: the MESA program performs well.

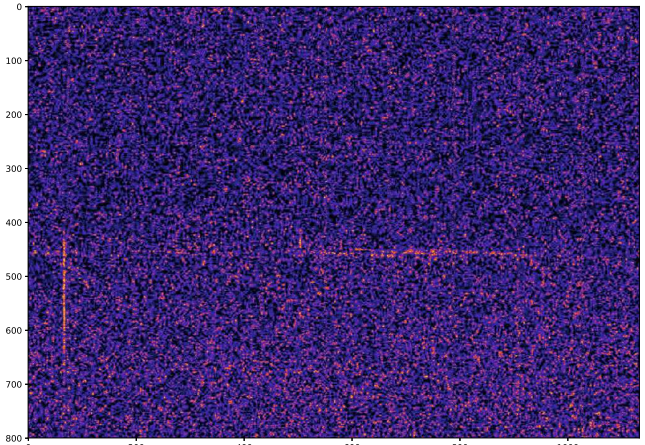

(b) Spectrogram with high noise.

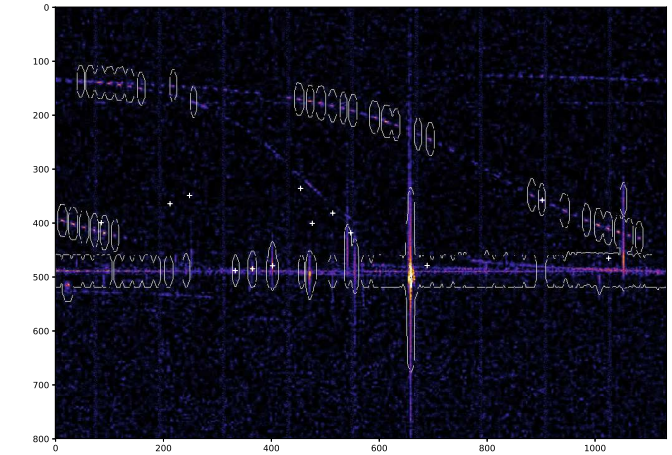

(c) Spectrogram containing artefacts from aeroplanes, and direct signal.

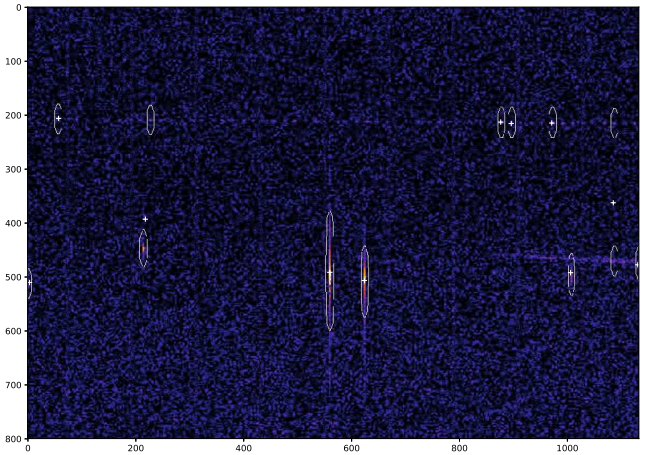

(d) Spectrogram containing tropospheric propagation.

Figure 14 – Examples of spectrograms and the performance of the MESA program on them.

higher-quality spectrograms, where the program will perform better, as demonstrated by the greater sensitivity at lower noise thresholds. Also, higher quality spectrograms will have fewer compression artefacts, which hinder performance. For example, the noise created by JPEG compression around the vertical time markers can cause false detections.

Resolution The resolution of the spectrogram image determines the resolution of the output data. Velocity data are displayed up to a resolution determined by the Hz-per-pixel value. Given a frequency resolution f_{err}, the velocity resolution is $\frac{c \cdot f_{\text{err}}}{f_0}$. The time resolution is determined by the seconds-per-pixel value.

Velocity calculation Calculation of velocity from a spectrogram is non-trivial and requires a detailed description of the detection geometry. In this paper we describe only a naïve method, which only gives accurate results for clearly defined head echoes that are simple structured, that is, conform to the expected 'streak' shape. However, identification of the head echo region may allow accurate calculation of velocity when more robust techniques and more detailed detection information available.

Colour scale Depending on the colour scale configuration, the greater intensity end of the scale may be saturated in the image (Figure 15) making the greater intensities indistinguishable by colour and consequently giving erroneous results.

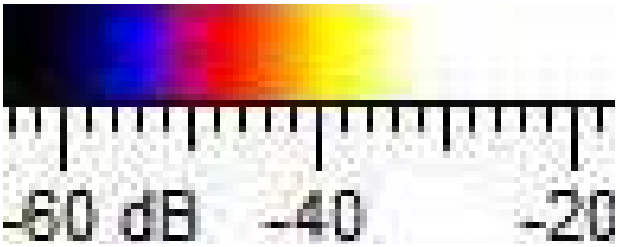

Figure 15 – CMRmap colour scale saturated at greater intensities

6.3 Advantages

Pipeline integration The MESA program can easily be integrated into a data pipeline, which offers an advantage over manual processing systems, even when many can contribute to the data analysis, for example the BRAMS Zooniverse project (Lamy et al., 2017). Data can be processed at a greater rate, with customisable settings, and there is less variation in analysis than when completed by multiple people.

Reliability Using an automated program ensures reliability when analysing multiple spectrograms, and even across multiple detection stations. This is extremely important when comparing data from multiple sources, and cannot always be guaranteed with other methods, especially manual analysis.

Historical data Detection stations often record data only in spectrogram format, since this requires far less memory storage than archiving the original radio signal. This backlog of data can be processed using MESA to give a large archive of detection counts and other data.

6.4 Future work

Adjustable sensitivity Most stages of the MESA program have adjustable settings: horizontal stretching factor (which is part of determining the time resolution), thresholding sensitivity, erosion and dilation strength, and CCA structural elements, TV Chambolle denoising weight, streak convolution kernel, and the outlier identification process. Combinations of certain parameters could be tested to give a powerful tool to detect certain elements of spectrograms: overdense or underdense meteors, for example. Thresholds could be set to only detect meteors above a given minimum intensity, or beyond a minimum duration.

Acceleration calculation Provided higher resolution spectrograms are available, the acceleration of an echo-producing meteor could be estimated by identifying the points of maximum and minimum velocity, and determining the time-separation of these points.

7 Conclusion

- Meteor head echoes may be automatically identified in spectrograms generated by forward-scatter radio detection, as well as bounding regions which allow calculation of further data including velocity and duration.
- Although the program does not perfectly replace manual processing, it allows significant reduction in the volume of data that must be manually processed.
- The MESA program allows large volumes of spectrogram data to be processed at a sensitivity of 0.790, with a greater sensitivity when low-noise data is processed: a sensitivity of 0.875 is attained with $\sim 65\%$ of the data below the noise threshold.
- This allows a consistent method of automatically identifying head echoes and the region that defines the echo.
- The program is easily extensible to allow automatic calculations relating to the echoes.
- Each step of the program is adjustable, so that the program can be customised for a given detection setup, or targeted at certain types of echoes.

Acknowledgements

This work has been funded by the Devon Cambridge Society. I am grateful to the Norman Lockyer Observatory for access to spectrogram data, and Michael Andrejczuk for suggestions and advice.

References

Chambolle A. (2004). "An algorithm for total variation minimisation and applications". *Journal of Mathematical Imaging and Vision*, **20:1-2**, 89–97.

Dillencourt M., Samet H., and Tamminen M. (1992). "A general approach to connected-component labeling for arbitrary image representations". *Journal of the ACM*, **39:2**, 253–280.

Gonzalez R. C. and Woods R. E. (2002). *Digital image processing*. Prentise Hall, New Jersey, 2 edition.

Lamy H., Calders S., Tétard C., Verbeeck C., Martinez Picar A., and Gamby E. (2017). "The Radio Meteor Zoo: searching for meteors in BRAMS radio observations". *European Planetary Science Congress*, **11**, EPSC2017–714.

Noguchi K. and Yamamoto M. (2008). "Development of an automatic echo-counting program for HROFFT spectrograms". *Earth, Moon, and Planets*, **102**, 323–329.

Otsu N. (1979). "A threshold selection method from gray-level histograms". *IEEE Trans. Sys., Man., Cyber.*, **9**, 62–66.

Roman V. and Buiu C. (2015). "Automatic detection of meteors in spectrograms using artificial neural networks". In *10th Jubilee IEEE Symposium on Applied Computational Intelligence and Informatics*. pages 131–134.

Šustr M. (2013). "Streak detection in astronomical images". Bachelor thesis, Center for Machine Perception, K13133 FEE Czech Technical University, Prague, Czech Republic, 38 pages.

Handling Editor: Jean-Louis Rault
This paper has been typeset from a LaTeX file prepared by the author.

Appendix

A Time-stamp indicator removal

Algorithm 1 Vertical timestamp-indicator line removal in pre-processing

```
img ← spectrogram after border removal
indices ← indices of columns with largest mean RGB pixel value in bottom pixel ▷ Ordered from largest to smallest
initialise lineLocations
imgNew ← deep copy of img
for i between 0, (length of indices) − 1 do
    ind ← column index at index i in indices
    imgNew ← img with column ind removed
    lineLocations ← ind − i
end for
```

B Broken region reconnection

Algorithm 2 Reconnection of broken echo regions

lbls ← array of region labels with same dimensions as spectrogram after pre-processing
for all region labels **do**
    com ← CoM of current region
    if *com* is a valid co-ordinate **then**
        x ← x co-ordinate
        y ← y co-ordinate
        rgnVal ← label of current region
        while region label at (x, y) = *rgnVal* **and** $x <$ image width **do**
            increment x
        end while
        rgnEnd ← x
        rgnStart ← index of *rgnVal* in array of row y
        column ← columns from x = *rgnStart* to x = *rgnEnd*
        otherRgns ← list of region labels (excluding *rgnVal* & 0) in the columns from *rgnStart* to *rgnEnd*
        for *labelVal* in *otherRgns* **do**
            replace all elements in *lbls* with region label *labelVal* **with** *rgnVal*
        end for
    end if
end for

C Maximum intensity calculation

Algorithm 3 Maximum intensity calculation

for i between 1, length of list of echo centres of mass **do**
    coords ← centre of mass for region with label i
    dims ← dimensions of region with label i
    scaleStart ← 0
    scaleEnd ← length in pixels of colour scale in image
    if *coms* is a valid co-ordinate **then**
        lbls ← array of region labels with same dimensions as image
        mask ← binary array where (x, y) in *mask* is 1 if (x, y) in *lbls* has value i, and 0 otherwise
        img_lbl_rgb ← copy of pre-processed image (after stretching, red channel extraction, line removal)
        replace elements of *img_lbl_rgb* corresponding to zeros in *mask* **with** 0
        initialise *scale_vals* **as** empty list
        for (*row*, *col*) in *img_lbl_rgb* **do**
            pxlVal ← *img_lbl_rgb* value at (*row*, *col*)
            if *pxlVal* non-zero **then**
                initialise *comparisons* **as** empty list
                for *scaleImgVal* in array of image values of scale **do**
                    $comp \leftarrow \left|\textbf{mean}\left(scaleImgVal - pxlVal\right)\right|$ ▷ Note subtraction is channel-wise, then mean is over the three channels
                    append *comp* **to** *comparisons*
                end for
                minIndex ← index of minimum value in *comparisons*
                $scaleVal \leftarrow \left[\frac{minIndex}{\text{length of } comparisons} \times (scaleStart - scaleEnd)\right] - offset$
            end if
        end for
    end if
end for

Preliminary results

Results of the IMO Video Meteor Network — March 2018, and annual minimum of meteor activity

Sirko Molau[1], *Stefano Crivello, Rui Goncalves, Carlos Saraiva, Enrico Stomeo, Jörg Strunk, Javor Kac*

During 2018 March, cameras of the IMO Video Meteor Network recorded over 10 000 meteors in nearly 6 200 hours of observing time. As March is typically the month of the lowest meteor activity for the Network cameras, data from 1999–2018 were examined to determine the precise annual minimum. The minimum meteor activity was found to occur at the end of March, which is tentatively attributed to the lowest declination of the Apex source occurring around that time. Activity of the Antihelion meteors is almost constant during the entire period studied (February to April).

Received 2019 March 7

A Introduction

In earlier years March was often the first highlight of the year with over 10 000 hours of effective observing time, but in March 2018 this was not the case (Table 1 and Figure 1). We have to look back as far as January 2014 to find a month in which we collected less than the around 6 200 hours of effective observing time. We barely recorded 10 000 meteors – the last time we recorded so few meteors was in June 2011!

The reason was not a lower number of active video cameras – overall 40 observers operated 78 cameras in March 2018. Our new Hungarian observer Henrietta Nagy even started to operate the new camera Hukon, but only 15 cameras managed to observe during twenty or more nights. In Slovenia the weather was particularly poor, but even our southern European observers in Italy and Spain which are typically spoiled by good weather conditions suffered significantly and barely managed twenty observing nights with their cameras.

The average rate dropped to 1.7 meteors per hour, which is the lowest annual activity, this being in line with the 1999–2018 long-term statistics of the IMO network (Figure 2).

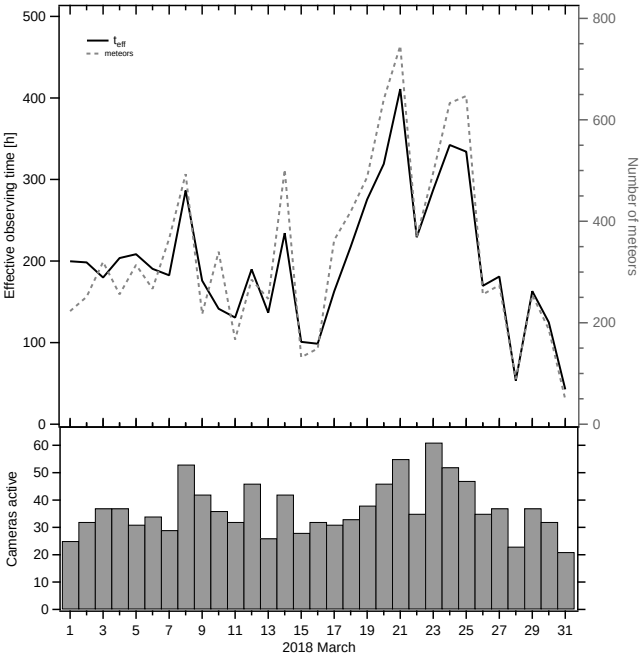

Figure 1 – Monthly summary for the effective observing time (solid black line), number of meteors (dashed gray line) and number of cameras active (bars) in 2018 March.

B Annual minimum of meteor activity

But when exactly is the point of lowest activity reached? To answer this question, we analyzed data from February to April for the years 2011–2018, for which we have flux density measurements. During that time of year we can observe sporadic meteors, the Antihelion source (which is actually also a sporadic source, but reported separately for historic reasons) but hardly any "real" meteor showers. During the time interval studied, the IMO working list (Rendtel, 2018) contains only the Lyrids and η-Aquariids towards the end of April. Otherwise there is no meteor shower activity for observers in mid-northern latitudes.

Let us have a closer look at the individual sources.

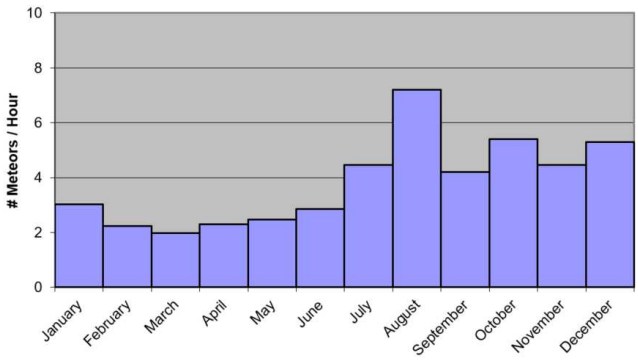

Figure 2 – Monthly mean number of recorded meteors per hour effective observing time in the years 1999–2018.

Figure 3 presents the temporal distribution of the average number of Antihelion meteors per hour. Each data point reflects 0.°1 solar longitude, the solid red line is the sliding mean over 2 degrees solar longitude. The

[1]Abenstalstr. 13b, 84072 Seysdorf, Germany.
Email: sirko@molau.de

IMO bibcode WGN-472-molau-vidmar
NASA-ADS bibcode 2019JIMO...47...66M

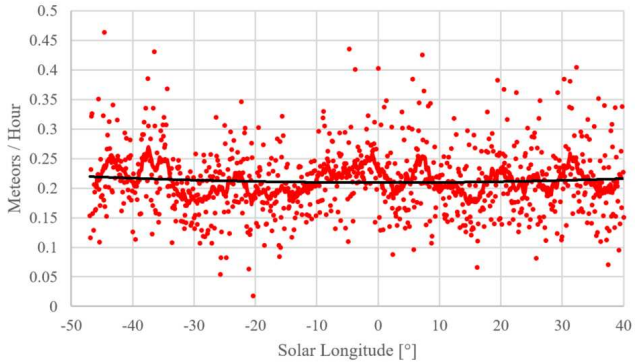

Figure 3 – Temporal distribution of the average number of recorded Antihelion meteors per hour effective observing time, derived from data of the IMO Video Meteor Network in 2011–2018.

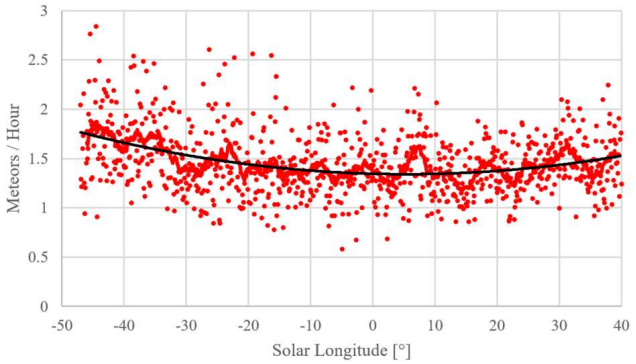

Figure 5 – Temporal distribution of the average number of recorded sporadic meteors per hour effective observing time, derived from data of the IMO Video Meteor Network in 2011–2018.

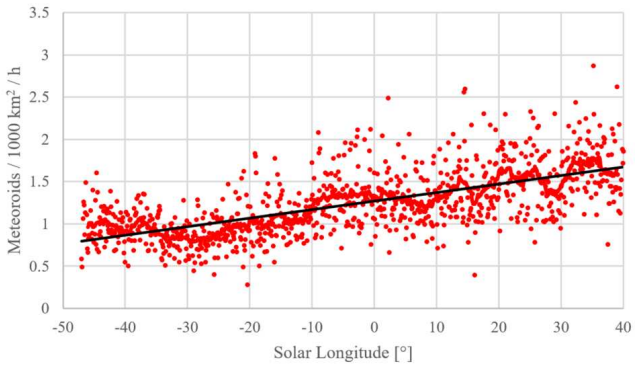

Figure 4 – Temporal distribution of the flux density of Antihelion meteors in 2011–2018.

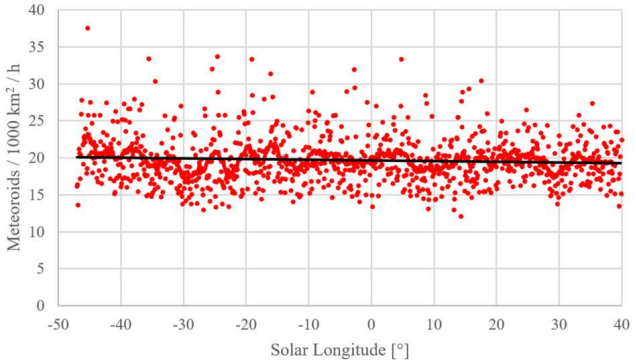

Figure 6 – Temporal distribution of the flux density of sporadic meteors in 2011–2018.

activity level is constant with one meteor every four to five observing hours. A quadratic fit (black line) is basically linear and parallel to the abscissa.

That is surprising, because the anti-solar point moves quickly from positive to negative declination around the vernal equinox, and the observing conditions for Antihelion meteors deteriorate. That is reflected by the flux density profile of the Antihelion source (Figure 4): The same number of meteors at a lower effective collection area implies a steady increase of the flux density. We have currently no better explanation than a real increase in particle density.

The picture looks different for sporadic meteors. Here we see the sought-after minimum in hourly meteor rates at the end of March (Figure 5). The activity drops down to 1.3 sporadic meteors per hour. A quadratic fit yields a minimum at 5° solar longitude, i.e. shortly after the vernal equinox. A possible explanation is quickly at hand: The Apex source makes up for a substantial part of the sporadic activity. It follows the Sun at an ecliptical longitude distance of 90° and reaches its lowest declination at the vernal equinox. Thus, the Apex "radiant" culminates end of March at the lowest possible altitude, which is why Apex meteors are particularly rare in spring.

MetRec calculates the flux density of sporadic meteors empirically as a weighted sum of individual sporadic sources (N/S Apex, Antapex, Helion, N/S Toroidal), whereby Apex has the biggest weight. Hence, it comes as no surprise that the sporadic flux density is constant in the analyzed time interval (Figure 6): The number of sporadic meteors drops proportional to the effective collection area, which implies a constant sporadic flux density.

Figure 7 shows the resulting average meteor count (Antihelion source, sporadic meteors and all meteor showers) per observing hour between February and April.

We can draw the following conclusions:

- Lowest hourly meteor counts (in the northern hemisphere) are reached at the end of March right after the vernal equinox.

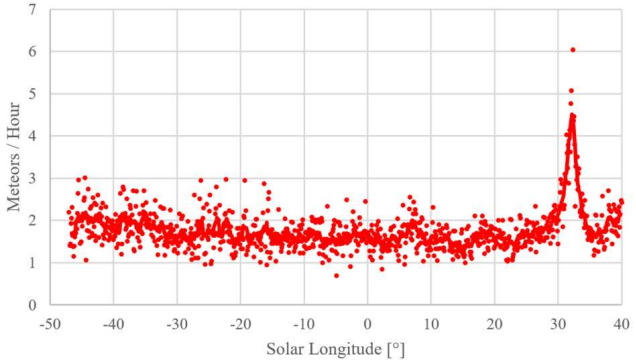

Figure 7 – Temporal distribution of the average number of recorded meteors per hour effective observing time, derived from data of the IMO Video Meteor Network in 2011–2018.

- The Apex source seems to be the dominating meteor source at this time of year. The low declination of the Apex would, at least, be a simple explanation for the observed minimum. To support this hypothesis, however, each meteor would have to be assigned to one of the individual sporadic sources or to the true random background activity.
- In the inspected time interval, the Antihelion source provides a constant number of meteors per observing hour, even though the observing geometry deteriorates quickly during the Spring.

References

Rendtel J. (2018). "2019 Meteor Shower Calendar". International Meteor Organization. IMO_INFO(2-18).

Handling Editor: Javor Kac

Code	Name	Location	Camera	FOV [°²]	Stellar LM [mag]	Eff.CA [km²]	Nights	Time [h]	Meteors
ARLRA	Arlt	Ludwigsfelde/DE	Ludwig2 (0.8/8)	1475	6.2	3779	20	112.1	289
BIATO	Bianchi	Mt. San Lorenzo/IT	Omsl1 (1.2/4)	6435	4.0	1705	14	16.4	107
BOMMA	Bombardini	Faenza/IT	Mario (1.2/4.0)	5794	3.3	739	25	137.4	303
BREMA	Breukers	Hengelo/NL	Mbb3 (0.75/6)	2399	4.2	699	13	27.4	86
BRIBE	Klemt	Herne/DE	Hermine (0.8/6)	2374	4.2	678	11	66.8	123
		Bergisch Gladbach/DE	Klemoi (0.8/6)	2286	4.6	1080	19	105.4	178
CARMA	Carli	Monte Baldo/IT	Bmh2 (1.5/4.5)*	4243	3.0	371	13	84.7	245
CASFL	Castellani	Monte Baldo/IT	Bmh1 (0.8/6)	2350	5.0	1611	9	60.7	90
CINFR	Cineglosso	Faenza/IT	Jenni (1.2/4)	5886	3.9	1222	21	25.0	169
CRIST	Crivello	Valbrevenna/IT	Arci (0.8/3.8)	5566	4.6	2575	20	95.2	211
			Bilbo (0.8/3.8)	5458	4.2	1772	19	89.5	183
			C3P8 (0.8/3.8)	5455	4.2	1586	16	82.3	161
			Stg38 (0.8/3.8)	5614	4.4	2007	16	86.1	244
ELTMA	Eltri	Venezia/IT	Met38 (0.8/3.8)	5631	4.3	2151	9	46.3	77
FORKE	Förster	Carlsfeld/DE	Akm3 (0.75/6)	2375	5.1	2154	9	62.8	102
GONRU	Goncalves	Foz do Arelho/PT	Farelho1 (0.75/4.5)	2286	3.0	208	16	75.8	46
		Tomar/PT	Templar1 (0.8/6)	2179	5.3	1842	21	106.4	176
			Templar2 (0.8/6)	2080	5.0	1508	21	109.1	197
			Templar3 (0.8/8)	1438	4.3	571	19	105.8	76
			Templar4 (0.8/3.8)	4475	3.0	442	19	90.5	159
			Templar5 (0.75/6)	2312	5.0	2259	21	99.8	137
GOVMI	Govedič	Središče ob Dravi/SI	Orion2 (0.8/8)	1447	5.5	1841	9	41.7	47
			Orion3 (0.95/5)	2665	4.9	2069	9	19.5	30
			Orion4 (0.95/5)	2662	4.3	1043	13	31.1	36
HERCA	Hergenrother	Tucson/US	Salsa3 (0.8/3.8)	2336	4.1	544	29	252.4	354
HINWO	Hinz	Schwarzenberg/DE	Hinwo1 (0.75/6)	2291	5.1	1819	17	82.8	103
IGAAN	Igaz	Budapest/HU	Hupol (1.2/4)	3790	3.3	475	6	37.1	12
JONKA	Jonas	Budapest/HU	Husor (0.95/4)	2286	3.9	445	14	78.0	56
			Husor2 (0.95/3.5)	2465	3.9	715	13	61.8	52
KACJA	Kac	Kamnik/SI	Cvetka (0.8/3.8)*	4914	4.3	1842	2	15.3	25
			Rezika (0.8/6)	2270	4.4	840	2	15.5	38
			Stefka (0.8/3.8)	5471	2.8	379	2	15.5	26
		Kostanjevec/SI	Metka (0.8/12)*	715	6.4	640	5	36.0	53
KOSDE	Koschny	Izana Obs./ES	Lic1 (2.8/50)*	2255	6.2	5670	5	23.2	69
LOJTO	Łojek	Grabniak/PL	Pav57 (1.0/5)	1631	3.5	269	7	49.8	138
MACMA	Maciejewski	Chełm/PL	Pav35 (0.8/3.8)	5495	4.0	1584	13	58.0	62
			Pav36 (0.8/3.8)*	5668	4.0	1573	17	104.2	160
			Pav43 (0.75/4.5)*	3132	3.1	319	15	95.3	41
			Pav60 (0.75/4.5)	2250	3.1	281	19	113.4	151

Table 1 – Observers contributing to 2018 March data of the IMO Video Meteor Network. Eff.CA designates the effective collection area; the overall number of nights is the number of nights with at least one camera operating, the overall observing time and number of meteors are sums over all cameras.

Table 1 – Observers contributing to 2018 March data of the IMO Video Meteor Network – continued from previous page.

Code	Name	Location	Camera	FOV [°²]	Stellar LM [mag]	Eff.CA [km²]	Nights	Time [h]	Meteors
MARRU	Marques	Lisbon/PT	Cab1 (0.75/6)	2362	4.8	1517	24	150.4	228
			Ran1 (1.4/4.5)	4405	4.0	1241	17	97.3	138
MOLSI	Molau	Seysdorf/DE	Avis2 (1.4/50)*	1230	6.9	6152	19	94.5	394
			Escimo2 (0.85/25)	155	8.1	3415	16	101.4	92
			Mincam1 (0.8/8)	1477	4.9	1084	14	72.5	188
		Ketzür/DE	Remo1 (0.8/8)	1467	6.5	5491	19	124.8	361
			Remo2 (0.8/8)	1478	6.4	4778	19	120.9	318
			Remo3 (0.8/8)	1420	5.6	1967	21	148.7	301
			Remo4 (0.8/8)	1478	6.5	5358	20	131.7	384
MORJO	Morvai	Fülöpszállás/HU	Huful (1.4/5)	2522	3.5	532	10	61.4	49
MOSFA	Moschini	Rovereto/IT	Rover (1.4/4.5)	3896	4.2	1292	16	81.1	90
NAGHE	Nagy	Budapest/HU	Hukon (0.8/3.8)	5500	4.0	1575	10	32.6	67
		Piszkéstető/HU	Hupis (0.8/3.8)	5615	4.0	1524	14	30.7	80
OCHPA	Ochner	Albiano/IT	Albiano (1.2/4.5)	2944	3.5	358	7	44.0	14
OTTMI	Otte	Pearl City/US	Orie1 (1.4/5.7)	3837	3.8	460	25	205.7	175
PERZS	Perkó	Becsehely/HU	Hubec (0.8/3.8)*	5498	2.9	460	14	41.2	99
ROTEC	Rothenberg	Berlin/DE	Armefa (0.8/6)	2366	4.5	911	12	92.2	83
SARAN	Saraiva	Carnaxide/PT	Ro1 (0.75/6)	2362	3.7	381	18	92.0	80
			Ro2 (0.75/6)	2381	3.8	459	18	101.4	128
			Ro3 (0.8/12)	710	5.2	619	17	105.8	173
			Ro4 (1.0/8)	1582	4.2	549	13	72.8	43
			Sofia (0.8/12)	738	5.3	907	17	68.3	94
SCALE	Scarpa	Alberoni/IT	Leo (1.2/4.5)*	4152	4.5	2052	10	33.4	42
SCHHA	Schremmer	Niederkrüchten/DE	Doraemon (0.8/3.8)	4900	3.0	409	19	107.8	137
SLAST	Slavec	Ljubljana/SI	Kayak1 (1.8/28)	563	6.2	1294	7	40.1	111
			Kayak2 (0.8/12)	741	5.5	920	7	34.0	24
STOEN	Stomeo	Scorze/IT	Min38 (0.8/3.8)	5566	4.8	3270	16	62.8	183
			Noa38 (0.8/3.8)	5609	4.2	1911	6	8.1	62
			Sco38 (0.8/3.8)	5598	4.8	3306	17	63.2	178
STRJO	Strunk	Herford/DE	Mincam2 (0.8/6)	2354	5.4	2751	22	110.9	304
			Mincam3 (0.8/6)	2338	5.5	3590	19	112.6	117
			Mincam4 (0.8/6)	2306	5.0	1412	21	98.8	116
			Mincam5 (0.8/6)	2349	5.0	1896	18	111.0	161
			Mincam6 (0.8/6)	2395	5.1	2178	14	105.7	143
TEPIS	Tepliczky	Agostyán/HU	Huago (0.75/4.5)	2427	4.4	1036	7	59.7	80
			Humob (0.8/6)	2388	4.8	1607	7	41.8	36
WEGWA	Wegrzyk	Nieznaszyn/PL	Pav78 (0.8/6)	2286	4.0	778	19	98.1	88
YRJIL	Yrjölä	Kuusankoski/FI	Finexcam (0.8/6)	2337	5.5	3574	20	148.4	221
ZAKJU	Zakrajšek	Petkovec/SI	Tacka (0.8/12)	714	5.3	783	8	48.3	45
* active field of view smaller than video frame						Overall	31	6 172.2	10 439

Results of the IMO Video Meteor Network — April 2018

Sirko Molau[1], Stefano Crivello, Rui Goncalves, Carlos Saraiva, Enrico Stomeo, Jörg Strunk, Javor Kac

Cameras of the IMO Video Meteor Network recorded over 18 500 meteors in almost 9 000 hours of observing time during 2018 April. The Lyrids were well observed and were found to peak during the night of 2018 April 22/23. Flux density and population index profiles are presented for this shower.

Received 2019 April 10

A Introduction

In April 2018, the number of active video cameras increased slightly, which is again thanks to our Hungarian observer Henrietta Nagy. With Huzan, she is now operating a third Mintron camera, this time equipped with a 6 mm $f/0.8$ c-mount lens. Overall 80 cameras enjoyed an unusually pleasant spring month, in which the weather conditions in Europe were somehow turned upside down. Cameras in northern Central Europe (Germany, Poland) which normally experience unsteady weather conditions enjoyed often up to 25 observing nights, whereas in the sun-kissed states of Southern Europe (Italy, Spain) the cameras were active on fewer nights. Two third of all cameras managed to observe during twenty or more observing nights, which is a threefold increase compared to March. In total we recorded over 18 500 meteors in almost 9 000 hours of effective observing time (Table 1 and Figure 1). That is the second-best April output ever, eclipsed only by April 2015 (Molau et al., 2015). It does not yet compensate for the poor start, but the year 2018 is at least catching up a bit.

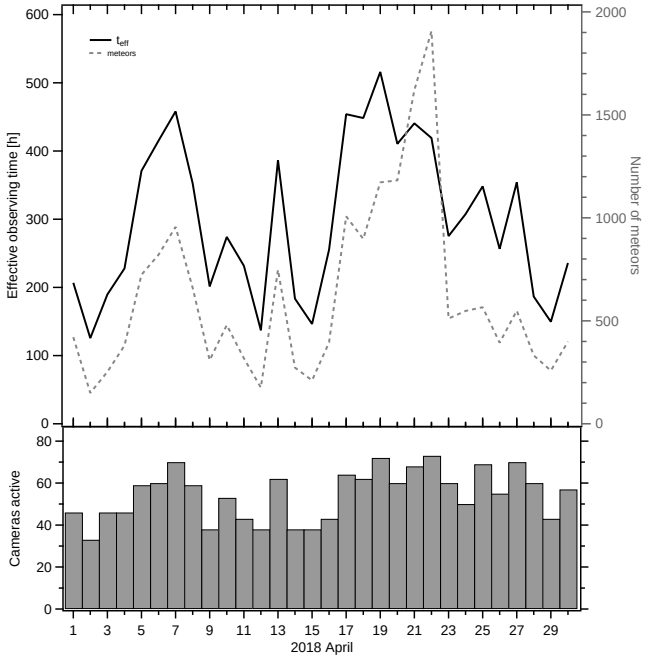

Figure 1 – Monthly summary for the effective observing time (solid black line), number of meteors (dashed gray line) and number of cameras active (bars) in 2018 April.

B Lyrids

The first relevant shower after the spring minimum is the Lyrids around April 22. Observing conditions for this shower were favorable this year, because the weather was often fine and the waxing Moon did not interfere with observations in the second half of night. Since the measured flux density was nearly identical during the nights before and after the peak (April 21/22 and 23/24, respectively) one could assume that we might have caught exactly the Lyrid peak on April 22/23. However, if the flux density of 2018 is projected onto the average profile of the years 2012–2017 (Figure 2) it becomes clear that we missed the peak in Central Europe by a few hours. The first meteors that night were recorded at 32.°4 solar longitude. The peak in the long-term video profile is positioned at 32.°17, which fell in the afternoon hours of 2018 April 22. This point in time is also somewhat earlier than given in the IMO Shower Workbook (32.°32 solar longitude) (Rendtel, 2014), and the observed 0.°6 solar longitude for the full width at half maximum (FWHM) is only half the size given by IMO Shower Workbook. However, the width of the Lyrids is also noted as being variable between half a day and two and a half days depending on the strength of the Lyrid peak. Times of half activity are positioned at about 32.°0 and 32.°6 solar longitude, which hints of an asymmetric activity profile with a steep ascending and a somewhat shallower descending branch. This can also be recognized visually in the activity profile.

The mean population index of the Lyrids is smaller by about 0.6 than the sporadic population index (Figure 3, left) if all data since 2012 are processed. However, it is difficult to analyze fine structures, because both profiles have the same shape. When the difference between them is calculated (Figure 3, right), we find a small peak at 32.°2 solar longitude at which difference is almost 1.0. Thus, the percentage of bright Lyrids is particularly high at the peak itself.

[1]Abenstalstr. 13b, 84072 Seysdorf, Germany.
Email: sirko@molau.de

IMO bibcode WGN-472-molau-vidapr
NASA-ADS bibcode 2019JIMO...47...71M

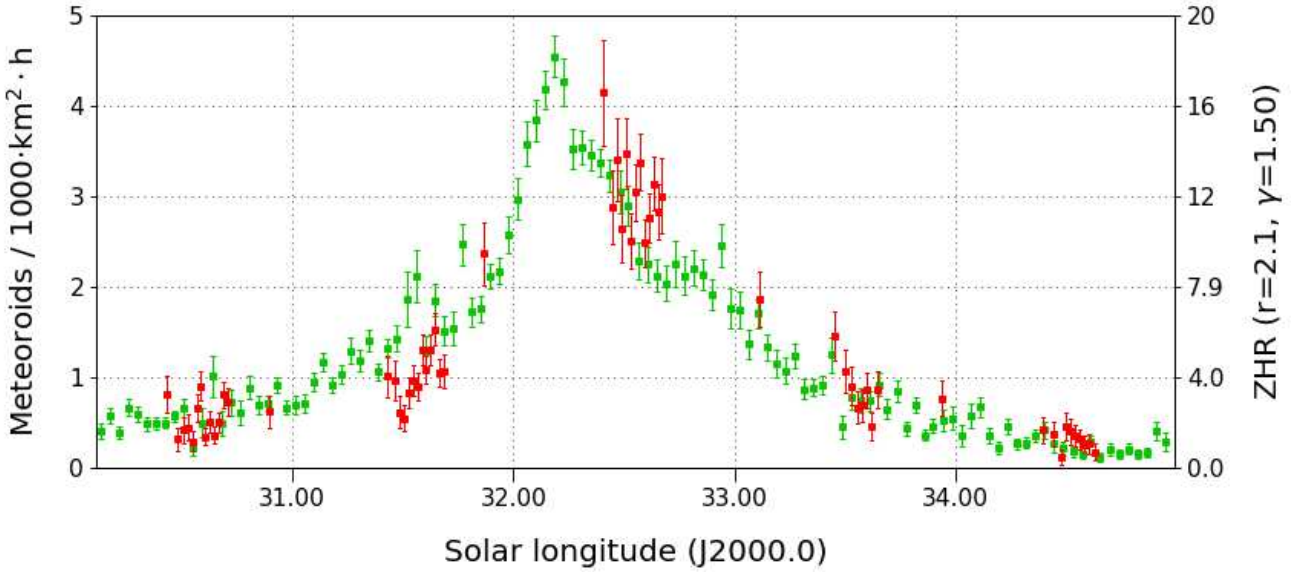

Figure 2 – Flux density profile of the Lyrids in 2018 April (lighter/green) and in the average of the years 2012–2017 (darker/red), derived from video data of the IMO Network.

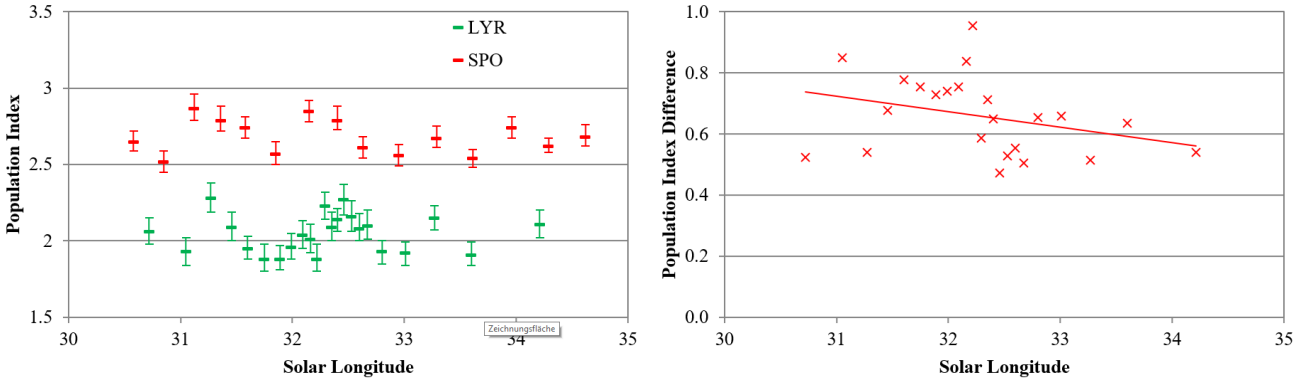

Figure 3 – Population index profile of the Lyrids and sporadic meteors in the average of the years 2012–2018 (left), and the difference between both profiles (right).

References

Molau S., Kac J., Crivello S., Stomeo E., Barentsen G., Goncalves R., Saraiva C., Maciejewski M., and Maslov M. (2015). "Results of the IMO Video Meteor Network – April 2015". *WGN, the Journal of the IMO*, **43:4**, 115–120.

Rendtel J. (2014). "Meteor shower workbook 2014". International Meteor Organization.

Handling Editor: Javor Kac

Code	Name	Location	Camera	FOV [°²]	Stellar LM [mag]	Eff.CA [km²]	Nights	Time [h]	Meteors
ARLRA	Arlt	Ludwigsfelde/DE	Ludwig2 (0.8/8)	1475	6.2	3779	26	126.6	419
BERER	Berkó	Ludányhalászi/HU	Hulud1 (0.8/3.8)	5542	4.8	3847	6	34.0	119
BIATO	Bianchi	Mt. San Lorenzo/IT	Omsl1 (1.2/4)	6435	4.0	1705	18	17.7	115
BOMMA	Bombardini	Faenza/IT	Mario (1.2/4.0)	5794	3.3	739	28	159.8	440
BREMA	Breukers	Hengelo/NL	Mbb3 (0.75/6)	2399	4.2	699	10	26.7	67
BRIBE	Klemt	Herne/DE	Hermine (0.8/6)	2374	4.2	678	23	125.9	225
		Bergisch Gladbach/DE	Klemoi (0.8/6)	2286	4.6	1080	22	134.2	208
CARMA	Carli	Monte Baldo/IT	Bmh2 (1.5/4.5)*	4243	3.0	371	24	163.4	613
CASFL	Castellani	Monte Baldo/IT	Bmh1 (0.8/6)	2350	5.0	1611	21	148.4	279
CINFR	Cineglosso	Faenza/IT	Jenni (1.2/4)	5886	3.9	1222	27	24.9	165
CRIST	Crivello	Valbrevenna/IT	Arci (0.8/3.8)	5566	4.6	2575	22	135.6	286
			Bilbo (0.8/3.8)	5458	4.2	1772	21	126.5	313
			C3P8 (0.8/3.8)	5455	4.2	1586	22	112.4	208
			Stg38 (0.8/3.8)	5614	4.4	2007	21	146.9	492
ELTMA	Eltri	Venezia/IT	Met38 (0.8/3.8)	5631	4.3	2151	18	118.1	283
FORKE	Förster	Carlsfeld/DE	Akm3 (0.75/6)	2375	5.1	2154	19	126.9	289
GONRU	Goncalves	Foz do Arelho/PT	Farelho1 (0.75/4.5)	2286	3.0	208	17	81.7	31
		Tomar/PT	Templar1 (0.8/6)	2179	5.3	1842	21	146.4	323
			Templar2 (0.8/6)	2080	5.0	1508	21	144.3	243
			Templar3 (0.8/8)	1438	4.3	571	21	138.4	88
			Templar4 (0.8/3.8)	4475	3.0	442	23	120.7	215
			Templar5 (0.75/6)	2312	5.0	2259	21	127.1	187
GOVMI	Govedič	Središče ob Dravi/SI	Orion2 (0.8/8)	1447	5.5	1841	23	127.3	202
			Orion3 (0.95/5)	2665	4.9	2069	16	73.0	79
			Orion4 (0.95/5)	2662	4.3	1043	16	53.0	111
HERCA	Hergenrother	Tucson/US	Salsa3 (0.8/3.8)	2336	4.1	544	27	224.6	263
HINWO	Hinz	Schwarzenberg/DE	Hinwo1 (0.75/6)	2291	5.1	1819	25	153.6	284
IGAAN	Igaz	Budapest/HU	Hupol (1.2/4)	3790	3.3	475	13	84.2	31
JONKA	Jonas	Budapest/HU	Husor (0.95/4)	2286	3.9	445	22	157.1	97
			Husor2 (0.95/3.5)	2465	3.9	715	24	135.2	149
KACJA	Kac	Kamnik/SI	Cvetka (0.8/3.8)*	4914	4.3	1842	13	90.1	322
			Rezika (0.8/6)	2270	4.4	840	14	88.7	459
			Stefka (0.8/3.8)	5471	2.8	379	13	91.7	224
		Kostanjevec/SI	Metka (0.8/12)*	715	6.4	640	10	31.4	107
KOSDE	Koschny	Izana Obs./ES	Lic1 (2.8/50)*	2255	6.2	5670	3	12.0	42
LOJTO	Łojek	Grabniak/PL	Pav57 (1.0/5)	1631	3.5	269	9	59.7	196
MACMA	Maciejewski	Chełm/PL	Pav35 (0.8/3.8)	5495	4.0	1584	25	107.7	194
			Pav36 (0.8/3.8)*	5668	4.0	1573	25	153.6	317
			Pav43 (0.75/4.5)*	3132	3.1	319	20	94.5	75
			Pav60 (0.75/4.5)	2250	3.1	281	26	164.2	325

Table 1 – Observers contributing to 2018 April data of the IMO Video Meteor Network. Eff.CA designates the effective collection area; the overall number of nights is the number of nights with at least one camera operating, the overall observing time and number of meteors are sums over all cameras.

Table 1 – Observers contributing to 2018 April data of the IMO Video Meteor Network – continued from previous page.

Code	Name	Location	Camera	FOV [°²]	Stellar LM [mag]	Eff.CA [km²]	Nights	Time [h]	Meteors
MARRU	Marques	Lisbon/PT	Cab1 (0.75/6)	2362	4.8	1517	14	85.1	127
			Ran1 (1.4/4.5)	4405	4.0	1241	17	111.3	136
MOLSI	Molau	Seysdorf/DE	Avis2 (1.4/50)*	1230	6.9	6152	28	152.4	803
			Escimo2 (0.85/25)	155	8.1	3415	26	146.9	308
			Mincam1 (0.8/8)	1477	4.9	1084	25	142.5	507
		Ketzür/DE	Remo1 (0.8/8)	1467	6.5	5491	27	127.7	454
			Remo2 (0.8/8)	1478	6.4	4778	25	128.1	462
			Remo3 (0.8/8)	1420	5.6	1967	25	148.9	401
			Remo4 (0.8/8)	1478	6.5	5358	27	145.9	598
MORJO	Morvai	Fülöpszállás/HU	Huful (1.4/5)	2522	3.5	532	23	26.2	114
MOSFA	Moschini	Rovereto/IT	Rover (1.4/4.5)	3896	4.2	1292	22	136.7	178
NAGHE	Nagy	Budapest/HU	Hukon (0.8/3.8)	5500	4.0	1575	24	105.5	242
		Piszkéstető/HU	Hupis (0.8/3.8)	5615	4.0	1524	25	122.3	263
		Zamárdi/HU	Huzam (0.8/6)	2358	4.7	1266	7	32.4	65
OCHPA	Ochner	Albiano/IT	Albiano (1.2/4.5)	2944	3.5	358	14	96.6	109
OTTMI	Otte	Pearl City/US	Orie1 (1.4/5.7)	3837	3.8	460	16	85.3	92
PERZS	Perkó	Becsehely/HU	Hubec (0.8/3.8)*	5498	2.9	460	18	98.6	99
ROTEC	Rothenberg	Berlin/DE	Armefa (0.8/6)	2366	4.5	911	22	123.9	159
SARAN	Saraiva	Carnaxide/PT	Ro1 (0.75/6)	2362	3.7	381	23	124.3	112
			Ro2 (0.75/6)	2381	3.8	459	24	141.5	163
			Ro3 (0.8/12)	710	5.2	619	23	144.7	197
			Ro4 (1.0/8)	1582	4.2	549	20	89.8	68
			Sofia (0.8/12)	738	5.3	907	19	61.6	94
SCALE	Scarpa	Alberoni/IT	Leo (1.2/4.5)*	4152	4.5	2052	19	107.4	113
SCHHA	Schremmer	Niederkrüchten/DE	Doraemon (0.8/3.8)	4900	3.0	409	22	110.3	154
SLAST	Slavec	Ljubljana/SI	Kayak1 (1.8/28)	563	6.2	1294	16	95.9	244
			Kayak2 (0.8/12)	741	5.5	920	18	124.3	99
STOEN	Stomeo	Scorze/IT	Min38 (0.8/3.8)	5566	4.8	3270	27	114.2	440
			Noa38 (0.8/3.8)	5609	4.2	1911	22	67.7	419
			Sco38 (0.8/3.8)	5598	4.8	3306	25	143.4	433
STRJO	Strunk	Herford/DE	Mincam2 (0.8/6)	2354	5.4	2751	25	136.2	376
			Mincam3 (0.8/6)	2338	5.5	3590	24	137.8	198
			Mincam4 (0.8/6)	2306	5.0	1412	22	124.7	150
			Mincam5 (0.8/6)	2349	5.0	1896	23	133.4	200
			Mincam6 (0.8/6)	2395	5.1	2178	23	123.5	197
TEPIS	Tepliczky	Agostyán/HU	Huago (0.75/4.5)	2427	4.4	1036	23	147.8	193
			Humob (0.8/6)	2388	4.8	1607	16	75.7	87
WEGWA	Wegrzyk	Nieznaszyn/PL	Pav78 (0.8/6)	2286	4.0	778	25	137.4	180
YRJIL	Yrjölä	Kuusankoski/FI	Finexcam (0.8/6)	2337	5.5	3574	14	62.9	121
ZAKJU	Zakrajšek	Petkovec/SI	Tacka (0.8/12)	714	5.3	783	21	155.3	176
* active field of view smaller than video frame						Overall	30	8 964.3	18 616

The International Meteor Organization

www.imo.net

Follow us on Facebook
InternationalMeteorOrganization

Follow us on Twitter
@IMOMeteors

Council

President: Cis Verbeeck,
Bogaertsheide 5, 2560 Kessel, Belgium.
e-mail: cis.verbeeck@scarlet.be

Vice-President: Juraj Tóth,
Fac. Math., Phys. & Inf., Comenius Univ.,
Mlynska dolina, 84248 Bratislava, Slovakia.
e-mail: toth@fmph.uniba.sk

Secretary-General: Robert Lunsford,
14884 Quail Valley Way, El Cajon,
CA 92021-2227, USA. tel. +1 619 755 7791
e-mail: lunro.imo.usa@cox.net

Treasurer: Marc Gyssens, Heerbaan 74,
B-2530 Boechout, Belgium.
e-mail: marc.gyssens@uhasselt.be
BIC: GEBABEBB
IBAN: BE30 0014 7327 5911
Bank transfer costs are always at your expense.

Other Council members:

Megan Argo, Jodrell Bank Centre for Astrophysics,
Alan Turing building, University of Manchester,
Oxford Road, Manchester, M13 9PL, UK.
e-mail: megan.argo@gmail.com

Javor Kac (see details under WGN)

Detlef Koschny, Zeestraat 46,
NL-2211 XH Noordwijkerhout, Netherlands.
e-mail: detlef.koschny@esa.int

Masahiro Koseki, 4-3-5 Annaka, Annaka-shi,
Gunma-ken 379-0116, Japan.
e-mail: geh04301@nifty.ne.jp

Sirko Molau, Abenstalstraße 13b, D-84072 Seysdorf,
Germany. e-mail: sirko@molau.de

Jean-Louis Rault, Société Astronomique de France,
16, rue de la Vallée, 91360 Epinay sur Orge,
France. e-mail: f6agr@orange.fr

Jürgen Rendtel, Eschenweg 16, D-14476 Marquardt,
Germany. e-mail: jrendtel@aip.de

Paul Roggemans, Pijnboomstraat 25, 2800 Mechelen,
Belgium, e-mail: paul.roggemans@gmail.com

Galina Ryabova, Res. Inst. of Appl. Math. & Mech.,
Tomsk State University, Lenin pr. 36, build. 27,
634050 Tomsk, Russian Federation.
e-mail: ryabova@niipmm.tsu.ru

Damir Šegon, J. Rakovca 3, 52100 Pula, Croatia.
e-mail: damir.segon@pu.t-com.hr

Commission Directors

Visual Commission: Rainer Arlt (rarlt@aip.de)
Generic e-mail address: visual@imo.net
Electronic visual report form:
http://www.imo.net/visual/report/electronic

Video Commission: Sirko Molau (video@imo.net)

Photographic Commission: Bill Ward
(William.Ward@glasgow.ac.uk)
Generic e-mail address: photo@imo.net

Radio Commission: Jean-Louis Rault (radio@imo.net)

Fireballs: Online fireball reports:
http://fireballs.imo.net

Outreach Officer

Jure Atanackov, e-mail: jureatanackov@gmail.com

Webmaster

Karl Antier, e-mail: webmaster@imo.net

WGN

Editor-in-chief: Javor Kac
Na Ajdov hrib 24, SI-2310 Slovenska Bistrica,
Slovenia. e-mail: wgn@imo.net;
include METEOR in the e-mail subject line

Editorial board: Ž. Andreić, M. Argo, D.J. Asher,
F. Bettonvil, J. Correira, M. Gyssens,
C. Hergenrother, T. Heywood, J.-L. Rault,
J. Rendtel, C. Verbeeck, S. de Vet, D. Vida.

IMO Sales

Available from the Treasurer or the Electronic Shop on the IMO Website	€	$
IMO membership, including subscription to WGN Vol. 47 (2019)		
Surface mail	26	32
Air Mail (outside Europe only)	49	60
Electronic subscription only	21	25
Proceedings of the International Meteor Conference on paper		
1990, 1991, 1993, 1995, 1996, 1999, 2000, 2002, 2003, per year	9	12
2007, 2010, 2011, per year	15	20
2012, 2013, 2014, 2015 per year	25	34
Proceedings of the Meteor Orbit Determination Workshop 2006	15	20
Radio Meteor School Proceedings 2005	15	20
Handbook for Meteor Observers	15	20
Meteor Shower Workbook	12	16
Electronic media		
Meteor Beliefs Project ZIP archive	6	8

2018 Geminids from Hum, Croatia